# Zirconia-supported Pt, Pd, Rh, Ru and Ni Catalysts in the Hydrotreatment of Fatty Amides and Amines

*Emma Verkama[1]*, Sylvia Albersberger[2], Kristoffer Meinander[3], Marja Tiitta[2], Reetta Karinen[1], Riikka L. Puurunen[1]*

*[1]Department of Chemical and Metallurgical Engineering, School of Chemical Engineering, Aalto University, P.O. Box 16100, 00076 Aalto, Finland*
*[2]Neste Corporation, P.O. Box 310, 06101 Porvoo, Finland*
*[3]Department of Bioproducts and Biosystems, School of Chemical Engineering, Aalto University, P.O. Box 16300, 00076 Aalto, Finland*

** Corresponding author:*
*Email: emma.verkama@aalto.fi*

## Abstract

Active catalysts for simultaneous hydrodeoxygenation (HDO) and hydrodenitrogenation (HDN) enable the production of fuels from renewable feedstocks. In this work, zirconia-supported nickel, ruthenium, rhodium, palladium and platinum catalysts were evaluated in the HDO and HDN of *n*-hexadecanamide (C16 amide). The HDN of 1-hexadecylamine (C16 amine) was studied separately to assess the HDN activity and preference between C–C and C–N bond cleavage routes without the interference of HDO. The differences in the catalytic activity were mainly attributed to the metal identity. $Pt/ZrO_2$ and $Ru/ZrO_2$ exhibited the highest activity towards the conversion of both model compounds. The C16 amide was converted more efficiently than the C16 amine over the studied catalysts, and a high HDO activity did not translate to a high activity in HDN, which was particularly evident in the case of $Rh/ZrO_2$. The active metal strongly influenced the preferred reaction routes, as observed from differences in the yields of C15 and C16 *n*-paraffins and C32 condensation products. $Ni/ZrO_2$ and $Pd/ZrO_2$ exhibited the lowest activity and paraffin selectivity in the hydrotreatment of both model compounds. $Ru/ZrO_2$ and $Rh/ZrO_2$ favored the formation of *n*-pentadecane from both the C16 amine and C16 amide, whereas $Pt/ZrO_2$ produced *n*-hexadecane and high intermediate yields of the C32 condensation products.

**Keywords:** hydrodenitrogenation, hydrodeoxygenation, amide, amine, noble metal catalyst

## 1. Introduction

Renewable fuels enable mitigating the $CO_2$ emissions of the heavy-duty transport sector and the aviation industry. Significant efforts have consequently been dedicated to research on the hydrotreatment of biobased feedstocks to renewable fuels, with a focus on hydrodeoxygenation (HDO), due to the significant oxygen content of biomass.[1–8] Some renewable feedstocks, such as animal fats and biocrudes obtained via hydrothermal liquefaction (HTL) of algae and sewage sludge, contain nitrogen in addition to oxygen.[9–14] Reducing the nitrogen content of such feedstocks via hydrodenitrogenation (HDN) is important, in parallel with HDO, as nitrogen-containing compounds are known to poison catalysts in downstream processing units and negatively impact the fuel stability.[15] While a complete oxygen removal can be obtained in the hydrotreatment of HTL biocrudes, HDN has been found to be more challenging, with the nitrogen removal often ranging between 50 and 80%.[16–19] There is, thus, a need to develop catalysts that are active for both HDO and HDN. Nevertheless, research on the HDN and HDO of molecules which contain both oxygen and nitrogen is limited,[20,21] despite the abundance of, e.g., fatty amides in renewable feedstocks.

Supported noble metal catalysts activate hydrogen in relatively mild conditions and are highly active for HDO reactions, especially via decarbonylation and decarboxylation routes.[5,22,23] Noble metal catalysts also exhibit activity towards C–N bond hydrogenolysis and are therefore an alternative to commercially used transition metal sulfide catalysts for the hydrotreatment of sulfur-free renewable feedstocks.[24–26] Considering the challenges encountered with the HDN of renewable feedstocks and the high activity of noble metal catalysts, it is relevant to study the activity of noble metal catalysts for simultaneous HDO and HDN.[16–19] The HDO and HDN of *n*-hexadecanamide (C16 amide, $C_{16}H_{33}NO$) to *n*-paraffins was recently studied on a series of supported Pt catalysts by Verkama et al.[27] The Lewis acid properties of the support markedly influenced the HDO activity and the selectivity towards the initial conversion route, but the HDN of the nitrogen-containing intermediate products and significant formation of secondary amines and amides limited the overall activity of the catalysts.[27] An inhibition of HDN by preferential HDO and condensation product formation has similarly been observed in the co-hydrotreatment of palmitic acid and 1-tetradecylamine over $Pt/ZrO_2$.[28]

In the hydrotreatment of fatty amides, the active metal can be expected to markedly influence the conversion of the amine intermediates.[25,29–33] The activity and selectivity between HDN and condensation of alkyl amines strongly depends on the active metal, which suggests that an appropriately chosen active

metal could enhance the paraffin yield and mitigate the formation of condensation products.[25,29–32] For example, Rh has been found to favor the formation of hydrocarbons in the hydrotreatment of methylamine, while secondary and tertiary amines readily are formed on Pd.[25,29–32] The metal identity also influences the activity and selectivity for the HDO of fatty acids and alcohols, i.e., the oxygen-containing compounds that are formed as intermediate products in the hydrotreatment of amides.[25,34] Here, Ru, Rh, Pd and Ni typically favor decarbonylation and decarboxylation routes, whereas Pt may favor C–O bond hydrogenolysis pathways, particularly if paired with a Lewis acidic support.[5,22,23,34–37] Considering the impact of the metal identity on the activity for HDN and HDO individually, it is of interest to investigate the effect of the active metal in the hydrotreatment of molecules that contain both oxygen and nitrogen.[27,28]

In this work, $ZrO_2$-supported Pt, Pd, Rh, Ru and Ni catalysts were studied in the hydrotreatment of the C16 amide and 1-hexadecylamine (C16 amine, $C_{16}H_{35}N$). $ZrO_2$ was selected as the catalyst support due to its mild Lewis acidity, which is beneficial for the hydrotreatment of amides.[27] The C16 amide was chosen as a model compound due to the presence of fatty amides in various biobased feedstocks, while the C16 amine was used to assess the HDN activity of the catalysts without the interference of simultaneous HDO.[9–11,24,38] The purpose of this work was to elucidate the impact of the active metal on the activity, selectivity and reaction routes in the hydrotreatment of fatty amides and amines, which to the best of our knowledge, has not been addressed before.

## 2. Experimental

2.1 Materials. Monoclinic zirconia ($ZrO_2$, SZ 31164, Saint-Gobain Norpro) was used as the catalyst support. The metal precursors were platinum(IV) nitrate solution (15 wt. % Pt), palladium(II) nitrate solution (12-16 wt. % Pd) and ruthenium(III) nitrosyl nitrate (31.78 wt. % Ru) from Alfa Aesar, as well as rhodium(III) nitrate solution (10 wt. % Rh) and nickel(II) nitrate hexahydrate (99.999% trace metals basis) from Aldrich.

For the reactor experiments, analytics, calibrations and catalyst characterization, the following chemicals were used: *n*-hexadecanamide (>95%) 1-hexadecylamine (>95%), *n*-hexadecanal (>97%), *n*-pentadecanonitrile (>95%) and *n*-heptadecanonitrile (>95%) from Tokyo Chemical Industry, *n*-pentadecane (>99%) from Aldrich, *n*-hexadecane (>99%), palmityl palmitate (>99%), decalin (decahydronaphthalene, anhydrous, mixture of cis and trans, >99%) and pyridine (anhydrous, 99.8%) from Sigma Aldrich, 1-hexadecanol (96%) from Acros Organics, palmitic acid (>98%) and 2-propanol (>99%) from Riedel de Haën, and *n*-dodecane (>99%) from Merck. The chemicals were used without further purification.

The hydrogen (99.995%) that was used in the reactor experiments and the nitrogen (99.999%), helium (99.999%), 2 vol. % $H_2$/Ar gas mixture (99.999%/99.999%) and 10 vol. % $CO_2$/He (99.999%/99.999%) gas mixture which were used for catalyst characterization, were purchased from Oy AGA Ab. The 10 vol. % CO/He gas mixture (99.999%/99.999%) was from Woikoski, and the helium (99.999%) and synthetic air (99.999%) used in the pyridine FTIR measurements were from Linde. The gases used for the product analysis; synthetic air (99.999%), helium (99.999%), hydrogen (99.999%), argon (99.999%) and oxygen (99.999%) were from Oy AGA Ab and Woikoski.

2.2 Catalyst Preparation. The catalysts were prepared with vacuum impregnation, targeting a 1 wt. % active metal loading. The $ZrO_2$-support was first crushed and sieved to a particle size of 0.25-0.42 mm. The support was then calcined in ambient air for 10 h at 600 °C in a static muffle furnace, and the impregnation was done as described previously.[28] The Ru, Rh, Pd and Ni catalysts were calcined in a flow-through calcination oven at 450 °C for 2 h using a 1 °C/min heating ramp, whereas the Pt catalyst was calcined at 450 °C for 1 h using a 2 °C/min heating ramp. A 100 ml/min flow of synthetic air was maintained throughout the calcination program.

2.3 Catalyst Characterization. The catalysts were characterized using similar methods as in a previous work by Verkama et al.[27] The method descriptions are repeated here for completeness. Isothermal $N_2$-physisorption measurements were carried out at -196 °C for the calcined catalysts and the $ZrO_2$ support, using a Surfer equipment from Thermo Scientific. Approximately 200 mg of sample was used for each measurement. Liquid nitrogen was used as a coolant. Before the analysis, the samples were degassed in vacuum at 350 °C for 180 min, using a 5 °C/min heating rate, with the purpose of removing moisture and other adsorbed compounds. After the measurements, dead volume calibrations were carried out with He. The Brunauer-Emmett-Teller (BET) method was used to calculate the specific surface area $S_{BET}$ ($m^2/g$) of each sample from the adsorption isotherm, while the Barrett-Joyner-Halenda (BJH) method was used for calculating the pore size distribution, mean pore diameter $d_{pore,}$ (nm) and pore volume $V_{pore}$ ($cm^3/g$) from the desorption branch.[39,40]

The active metal loadings (wt. %) were measured semi-quantitatively with X-ray fluorescence (XRF). The measurements were conducted with a wavelength dispersive PANalytical Axios mAx equipment. Approximately 200 mg samples of the calcined catalysts were ground for the analysis and measured as loose powders in He. The powders were placed in Chemplex 1330-SE sample cups, which were covered with a 3.6 µm mylar film.

The crystallographic phase of the calcined catalysts was identified with X-ray diffraction (XRD) measurements. The measurements were carried out with a PANalytical X'Pert PRO MPD Alpha-1 X-ray diffractometer, with Cu Kα1 radiation (45 kV, 40 mA). The measurements were conducted for a 2θ scanning range spanning between 5° and 100° (0.026° step size). The phase identification was performed with the HighScore software (ICDD PDF-4+ 2023 database).

Scanning transmission electron microscopy (STEM) analysis was conducted for the calcined catalysts. The measurements were carried out with a JEOL JEM-2200FS aberration corrected high resolution electron microscope, which was operated at an acceleration voltage of 200 kV. Before the analysis, the samples were drop-casted with acetone on copper grids and coated with ultrathin carbon film. Elemental mappings were carried out with an X-ray energy-dispersive spectrometer (EDS) which was coupled to the microscope. For the Rh and Pt catalysts, the diameter of approximately 100 metal particles were measured using the ImageJ software, in order to analyze the particle size distribution and the average Pt and Rh particle size.

Pulse chemisorption measurements were carried out for 100 mg catalyst samples to estimate the mean metal particle size and dispersion. CO was used as a probe molecule for $Ru/ZrO_2$, $Pt/ZrO_2$ and $Pd/ZrO_2$, whereas $H_2$ was used for $Ni/ZrO_2$ and $Rh/ZrO_2$. The measurements were done in an AMI-200R flow through equipment (Altamira Instruments), which was connected to an OmniStar GSD320 mass spectrometer (MS) (Pfeiffer Vacuum).

Before the pulse chemisorption, the samples of the calcined catalysts were first dried for 120 min at 200 °C in He and reduced for 60 min at 350 °C in 2 vol. % $H_2$/Ar. The samples were then cooled down to 50 °C and flushed in He for 60 min. Next, in case of CO pulse chemisorption, 25 pulses (0.505 ml) of 5 vol. % CO/He, were introduced to the samples with 5 min intervals. The composition of the outlet gas was analyzed with the MS (*m/z* 28 for CO, 44 for $CO_2$ and 18 for $H_2O$). In the case of $H_2$ pulse chemisorption, 15 pulses (0.505 ml) of 4 vol. % $H_2$ were introduced to the samples with 10 min intervals, while monitoring *m/z* 2 for $H_2$ with the MS. The temperature of the pulse loop was 100 °C during the CO pulse chemisorption measurements, and 30 °C during the $H_2$ pulse chemisorption measurements. A constant carrier gas flow of 50 ml/min (STP) was kept throughout the measurement. The relations presented in the Handbook of Heterogeneous Catalysis were used to estimate the dispersion $D$ (%) and mean particle size $d_m$ (nm) from the adsorbed amount of probe gas.[41] An adsorption stoichiometry of 1 was assumed for CO, whereas the adsorption stoichiometry for $H_2$ was assumed to be 2.

Hydrogen temperature-programmed reduction ($H_2$-TPR) was performed for 120 mg samples of the calcined catalysts to study the reduction temperatures of the metals. The measurements were done in the AMI-200R tool. The samples were heated in He from room temperature to 200 °C and maintained at 200 °C for 120 min, in order to remove moisture. A 10 °C/min heating rate was used. Afterwards, the samples were cooled down to 30°C in He. Once the temperature reached 30 °C, the samples were flushed for 30 min in Ar, after which a flow of 2 vol. % $H_2$/Ar was directed through the samples, and the temperature was elevated to 600 °C using a 5 °C/min heating rate. A constant carrier gas flow of 50 ml/min (STP) was kept through the measurement. In the data treatment and visualization, the $H_2$-TPR data between 30 °C and 50 °C was discarded, as the gas flowrate had not fully stabilized. The outlet gas was analyzed with the OmniStar GSD320 MS, and *m/z* 2 was followed to monitor the $H_2$ consumption. Additionally, *m/z* 4 (He), 18 ($H_2O$), 28 ($N_2$/CO), 32 ($O_2$) and 40 (Ar) were followed.

X-ray photoelectron spectroscopy (XPS) of the catalysts was carried out using a Kratos AXIS Ultra DLD X-ray photoelectron spectrometer with a monochromated $Al_{K\alpha}$ X-ray source (1486.7 eV) run at 100 W. Photoelectrons were collected at a 90° take-off angle, using a pass energy of 80 eV and step size of 1.0 eV for surveys and a pass energy of 20 eV and step size of 0.1 eV for high-resolution spectra. The area of analysis was 300 µm x 700 µm, using an X-ray beam spot with a diameter of 1 mm. The base pressure of the vacuum system was below 1 x $10^{-9}$ Torr. Spectra were collected from three different spots on each sample. High-resolution spectra were charge-corrected to a position of C–C bonding at 284.8 eV. All analysis of the measured spectra was carried out using the CasaXPS software. Prior to XPS measurements, the catalyst samples were reduced ex situ at 350 °C in 2 vol. % $H_2$/Ar for 60 min after which they were transferred to the vacuum system through air.

The Zr 3d spectra were fitted with two doublets, with the $3d_{5/2}$ peaks located at 181.8 eV and 183.0 eV. The lower binding energy component corresponds to a pure metal oxide, while the higher binding energy component was assigned to a mixed oxide state with a slightly lower electron density surrounding the Zr ions. The O 1s spectra were deconvoluted using three Gaussian components with equal full width at half maximum (FWHM). The most prevalent component corresponds to lattice oxygen of the support, followed by a component attributed to surface hydroxyls at a slightly higher binding energy (+1.5 eV). Furthermore, a minor component at higher binding energies (approximately 533.3 eV) was used, most likely attributed to oxygen bound to organic contaminants. The C 1s spectra were fitted with four Gaussian components based on standard tabulated chemical shifts. The peak positions at 284.8 eV (C–C), 286.5 eV (C–O), 287.8 eV (C=O), and 288.9 eV (O–C=O), corresponded to adventitious carbon. For the $Ru/ZrO_2$ catalyst, a deconvolution of the C 1s components was done together with the Ru 3d components, due to the overlap in the binding energy for these photoelectrons.

The Pt 4f spectrum of the $Pt/ZrO_2$ catalyst was fit using five doublets. These were related to metallic Pt(0), Pt (I), Pt(II), Pt(IV), and to a mixed state located between Pt(I) and Pt(II). The binding energies for the Pt $4f_{7/2}$ of these components were located at 70.9 eV, 72.1 eV, 73.4 eV, 74.4 eV, and 72.4 eV, respectively. Fixed energy separations and full-width-half-maximum (FWHM) were used for all components in the spectra. The mixed state is very close in energy to the Pt(I) state, but it was necessarily introduced as a single peak with fixed FWHM at approximately that energy was not sufficient to give a good final fit to the spectra. The Pd 3d spectrum of the $Pd/ZrO_2$ catalyst was fit with two doublets at $3d_{5/2}$ energies at 335.3 eV and 336.8 eV, corresponding to metallic Pd(0) and Pd(II). The Pd 3d spectrum overlaps with the Zr 3p

spectrum, but the Pd $3d_{1/2}$ component was clearly visible between the peaks for the Zr 3p doublet, thereby allowing for the deconvolution of the smaller palladium components. The Ni 2p spectrum of the Ni/$ZrO_2$ catalyst was deconvoluted using three components corresponding to Ni(0), Ni(II) and Ni(III), with the $2p_{3/2}$ peaks at energies 852.8 eV, 853.9 eV, and 856.3 eV, respectively, coupled together with three broader satellite features at higher energies.[42] All main components had similar FWHM, and fixed energy separations. The lowest energy component is consistent with what would be expected for metallic Ni, while the two higher energy components can both be associated with different degrees of oxidation. Two doublets were used to deconvolute the Rh 3d spectrum of the Rh/$ZrO_2$ catalyst, at $3d_{5/2}$ energies of 307.2 eV and 308.8 eV, corresponding to Rh(0) and Rh(III). The deconvolution of the Ru 3d spectrum of the Ru/$ZrO_2$ catalyst was complicated by the overlap with the C 1s spectrum. Two doublets with the $3d_{5/2}$ energies at 279.8 eV and 280.9 eV were used, corresponding to Ru(0) and Ru(IV), respectively. The binding energies of the transition metals components were in agreement with values given for similar components in the NIST database.[43] For all transition metals, apart from the Ni 2p region, fitting was done to both spin-orbit doublets. Fixed area ratios, energy separations and FWHM were used for each separate core level.

The overall basicity of the calcined catalysts and the $ZrO_2$ support was characterized through temperature-programmed desorption of $CO_2$ ($CO_2$-TPD). The analysis was done with the AMI-200R equipment for 150 mg catalyst samples. The samples were first dried for 120 minutes at 180 °C in He (10 °C/min heating rate), and cooled down to 50 °C. The samples were held at 50 °C in He for 30 min. A flow of 1 vol. % $CO_2$/He flow was then directed through the samples at 50 °C and held for 30 min. This was followed by a 60 min flush in He. The temperature was then elevated to 800 °C in He flow, using a heating rate of 10 °C/min. The temperature was maintained at 800 °C for 30 min before the samples were cooled down. The OmniStar GSD320 MS was used for data acquisition, and *m/z* 44 was followed for $CO_2$. Additionally, *m/z* 28 (CO), 18 ($H_2O$), 32 ($O_2$) and 4 (He) were followed. The carrier gas flow was kept constant at 50 ml/min (STP) throughout the measurement.

Acid site characterization was carried out for the calcined catalysts with Fourier transform infrared spectroscopy (FTIR), using pyridine as the probe molecule. The measurements were carried out with a Thermo Scientific Nicolet iS10 spectrometer, which was equipped with an in situ transmission FTIR cell by Harrick Scientific Products Inc (customized from the HTC-3 model), a liquid-$N_2$ cooled Mercury-Cadmium-Telluride (MCT) detector and a HeNe laser. A spectral range of 4000-650 $cm^{-1}$ (0.24 $cm^{-1}$ resolution) were used.

A hydraulic press was used to shape the samples of the calcined catalysts (25 mg) into self-supported pellets with a diameter of 1.1 cm. The samples were pretreated by heating in vacuum, first at 90 °C for 30 minutes (5 °C/min heating rate), and then at 450 °C for 60 minutes (20 °C/min heating rate). The samples were then cooled down to 170 °C and held for 10 min. Next, the spectra of the clean samples were collected. The samples were then saturated with pyridine for 10 min, using an atmospheric saturator. After the saturation, the samples were evacuated and held for 15 minutes. The spectra that were used to quantify the acidity were collected after the evacuation.

The Omnic 9.11 software was used for data processing. The background and the spectra of the clean samples were subtracted from the spectra of the pyridine-saturated samples, and the peak areas were integrated. OriginPro was used to deconvolute the spectra. The peak areas and sample weights were used to estimate the concentration of Lewis and Brønsted acid sites, as described by Emeis.[44]

2.4 Catalytic Activity Tests. The catalytic activity tests were performed in a 100 ml Hastelloy high-pressure batch reactor by Parr Instrument Company. The experimental conditions were similar as in previous works by Verkama et al.[27,28]

A 20 mg catalyst sample was first dried in situ for 60 min at 180 °C under 10 bar of $N_2$, and then reduced for 60 min at 350 °C under 20 bar of $H_2$. The feed mixtures were prepared by dissolving 56.5 mg of *n*-hexadecanamide or 53.5 mg of 1-hexadecylamine to 31 ml of decalin under heating. An initial nitrogen concentration of 100 ppm was targeted. A 1 ml zero-sample was collected for analysis, and the feed mixture was transferred to the heated feed vessel attached to the reactor. The reactor was heated to 300 °C, and the feed mixture was released to the reactor from the feed vessel. The rector was then pressurized to 80 bar $H_2$ and stirring at 600 rpm was initiated. The reaction was quenched with ice and the stirring was stopped, once the reaction time (15-300 min) had elapsed. A reference reaction time of 60 min was used to compare the catalysts and model compounds. The reactions with different reaction times were visualized as a function of batch residence time τ ($g_{cat}h/g_{amide}$), as defined in Equation (1), to account for any differences in the amounts of catalyst and reactant.

$$\tau = \frac{m_{\mathrm{cat}} t}{m_{\mathrm{A}}} \qquad (1)$$

Here, $m_{cat}$ (g) is the catalyst weight, $t$ (h) is the reaction time and $m_A$ (g) is the weight of reactant at the start of the reaction.

Thermal tests and experiments with the bare $ZrO_2$ support were done for both model compounds. A set of control experiments, described and reported in a previous work by Verkama et al.,[27] were carried out for the $Pt/ZrO_2$ catalyst.

2.5 Analysis of the Liquid Reaction Products. A second solvent (2-propanol) and an internal standard (*n*-dodecane) were added to the samples prior to analysis. The second solvent was added to prevent precipitation of the reactant and the products.

The products were identified with gas chromatograph-mass spectrometry (GC-MS), as explained previously.[28]

Quantification of the liquid products was carried out with an Agilent 7890 gas chromatograph (GC), equipped with an Agilent J&W HP5-MS column (30 m × 0.25 mm × 0.25 µm). The outlet of the column was split to a flame ionization detector (FID) and a nitrogen phosphorus detector (NPD). The inlet temperature of the GC, the temperature of the FID and the temperature of the NPD were 325 °C. The injection volume was 2 µl and the split ratio was 5:1. The analysis program started with a 3 min hold at 40 °C. The temperature was then raised to 100 °C with a ramp of 20 °C/min and held at 100 °C for 3 min. Next, the temperature was elevated to 150 °C with a ramp of 5 °C/min, and to 325 °C with a ramp of 10 °C/min. The temperature was held at 325 °C for 12 min. The calibrations were done as described previously by Verkama et al.[27]

The conversion of the reactant, $X_A$ (%), was calculated with Equation (2),

$$X_A = \frac{n_{A,0} - n_A}{n_{A,0}} \cdot 100\%, \quad (2)$$

where $n_{A,0}$ (mol) is the initial amount of reactant and $n_A$ (mol) is the amount of unreacted reactant in the product sample.

The product yields $Y_P$ (%) were calculated with Equation (3),

$$Y_{\mathrm{P}} = \frac{\mu_{\mathrm{P}} n_{\mathrm{P}}}{n_{\mathrm{A},0}} \cdot 100\%, \quad (3)$$

where $\mu_P$ is a stoichiometric factor ($\mu_P$ = 2 in case of the C32 compounds, $\mu_P$ = 1 for the other compounds) and $n_P$ (mol) is the amount of product *P* in the sample.

The oxygen removal (*O-removal*, %) of the C16 amide experiments was estimated from the product distribution, according to Equation (4),

$$O\text{-}removal = \frac{c_{\mathrm{O,products}}}{c_{\mathrm{O,feed}}} \cdot 100\%, \quad (4)$$

where $c_{O,\ products}$ (ppm) and $c_{O,\ feed}$ (ppm) are the oxygen contents of the product sample and feed mixture, respectively, based on the amounts of oxygen-containing compounds that were detected from the GC-FID analysis.

The carbon balance closure $B_C$ (mol. %) was obtained with Equation (5),

$$B_{\mathrm{C}} = \frac{n_{\mathrm{C,products}}}{n_{\mathrm{C,feed}}} \cdot 100\%, \quad (5)$$

where $n_{C,\ products}$ (mol) and $n_{C,\ feed}$ (mol) are the amounts of carbon quantified from the product sample from the sample of the feed mixture, respectively. The carbon balance closure of the catalytic experiments typically exceeded 90 mol. %.

An AntekPAC ElemeNtS analyzer was used to measure the nitrogen content of the liquid samples. The device was calibrated for nitrogen contents between 0 and 1000 ppm, using standard calibration solutions acquired from AC Analytical Controls BV. The results were used to calculate the nitrogen removal (*N-removal,* %) as presented in Equation (6),

$$N\text{-}removal = \frac{c_{\mathrm{N,products}}}{c_{\mathrm{N,feed}}} \cdot 100\%, \quad (6)$$

where $c_{N,\ products}$ (ppm) is the nitrogen content of the product sample and $c_{N,\ feed}$ (ppm) is the nitrogen content of the feed mixture.

2.6 Gas Phase Analysis. A gas phase sample was collected to a bomb after the reactor had cooled down. The gas phase was qualitatively analyzed with an Agilent 6890 permanent gas GC. Non-condensable gases were separated with HP-PLOT and HP-Molesieve columns, using Ar as the carrier gas, and were detected with a TCD. The hydrocarbons were separated with a HP-AL/KCL column using He as the carrier gas and detected with an FID. Each sample was analyzed three times.

## 3. Results and Discussion

**3.1 Catalyst Characterization.** Table 1 displays the BET specific surface area, pore volume and mean pore diameter obtained from $N_2$-physisorption measurements of the calcined catalysts, and the CO or $H_2$ adsorption capacity, mean metal particle size and dispersion obtained from pulse chemisorption measurements of the reduced catalysts.

**Table 1.** Properties of the catalysts based on $N_2$-physisorption measurements and pulse chemisorption measurements

| Catalyst | $N_2$-physisorption[a] | | | Pulse chemisorption[b] | | |
|---|---|---|---|---|---|---|
| | $S_{BET}$ ($m^2/g$) | $V_{pore}$ ($cm^3/g$) | $d_{pore}$ (nm) | CO/$H_2$ ads. capacity ($\mu mol/g_{cat}$) | $d_m$ (nm) | $D$ (%) |
| $ZrO_2$ | 47 | 0.25 | 20 | - | n.a. | n.a. |
| $Ni/ZrO_2$ | 48 | 0.23 | 20 | 3[d] | 30[d] | 4%[d] |
| $Pd/ZrO_2$ | 50 | 0.27 | 19 | 36[c] | 2.9[c] | 38%[c] |
| $Pt/ZrO_2$ | 42 | 0.25 | 19 | 30[c] | 1.9[c] | 59%[c] |
| $Rh/ZrO_2$ | 45 | 0.23 | 20 | 25[d] | 2.2[d] | 50%[d] |
| $Ru/ZrO_2$ | 48 | 0.26 | 20 | 61[c] | 2.1[c] | 61%[c] |

[a] The measurements carried out for the calcined catalysts
[b] The catalysts were reduced at 350 °C in $H_2$ before the measurements
[c] Based on CO pulse chemisorption
[d] Based on $H_2$ pulse chemisorption
n.a. = not applicable

The semi-quantitative XRF analysis indicated a metal loading of 0.6 wt. % for $Pd/ZrO_2$ and $Pt/ZrO_2$, and a metal loading of 0.7 wt. % for $Ni/ZrO_2$, $Rh/ZrO_2$ and $Ru/ZrO_2$. These values were within the measurement uncertainty of each other. The $N_2$-physisorption isotherms of the catalysts resembled Type IV(a) of the IUPAC classification, with a Type H2(b) hysteresis loop.[46] The BET specific surface area (42-50 $m^2/g$), pore volume (0.23-0.27 $cm^3/g$) and mean pore diameter (19-20 nm) of the catalysts and the bare support were similar, indicating that impregnation of the active metal did not alter the morphology of the support significantly (Table 1). The $N_2$-physisorption isotherms and BJH pore size distribution of the catalysts and the support are displayed in Figure S1 and Figure S2 of the Supporting Information. The X-ray diffractograms of the calcined catalysts only contained reflections related to monoclinic $ZrO_2$ (ICDD 00-007-0343), suggesting that the active metals were well dispersed before reduction.[47] The X-ray diffractograms of the calcined catalysts and the $ZrO_2$ support are available in Figure S3 of the Supporting Information.

The reduction temperatures of the active metals were studied via $H_2$-TPR measurements of the calcined catalysts. The $H_2$-TPR profiles of the catalysts and the $ZrO_2$ support are presented in Figure 1.

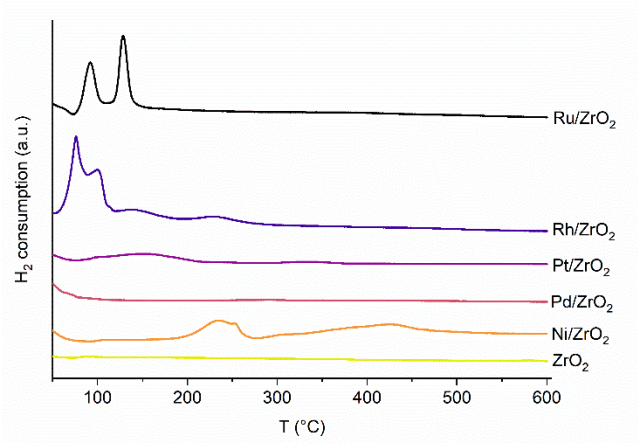


**Figure 1.** $H_2$-TPR profiles of the calcined catalysts and the $ZrO_2$ support. The data has been vertically shifted for clarity.

No reducible species were detected on the bare $ZrO_2$ support (Figure 1). The $H_2$-TPR profile of $Ni/ZrO_2$ had three major reduction peaks. The first and second peaks reached their maximum intensity at 237 °C and 257 °C, respectively. The third broad and shallow reduction peak reached its maximum intensity at 425 °C, i.e., above the reduction temperature that was used for the activity tests (350 °C). The first reduction peaks were likely related to the reduction of NiO particles with relatively weak interactions with the $ZrO_2$ support.[37,48–50] The higher temperature peak may have involved the reduction of NiO particles interacting more strongly with the $ZrO_2$ support, or the reduction of $Ni^{2+}$ species in the $ZrO_2$ lattice.[37,48–50] It is possible that a part of the Ni remained oxidic at the end of the $H_2$-TPR measurement.[51]

The $H_2$-TPR profile of $Pd/ZrO_2$ did not contain any major reduction peaks, but the $H_2$ consumption signal was elevated from the start of the ramp until approximately 100 °C (Figure 1). This could suggest that the PdO got reduced immediately upon the introduction of $H_2$, or that the Pd was in its reduced state already after calcination.[52] The $H_2$ consumption at low temperatures on all samples might also be related to $H_2$ adsorption or spillover.

The $H_2$-TPR profile of $Pt/ZrO_2$ contained a broad and shallow reduction peak around 140 °C, which probably involved the reduction of $PtO_2$ to metallic Pt (Figure 1).[53,54] Multiple reduction peaks were present in the $H_2$-TPR profile of $Rh/ZrO_2$.The reduction of $Rh_2O_3$ particles to metallic Rh mainly occurred

below 130 °C, as observed from the major reduction peaks at 75 and 98 °C.[55–59] The two smaller reduction peaks at 140 and 230 °C may have been attributed to reduction of larger $Rh_2O_3$ particles, $Rh_2O_3$ particles interacting more strongly with the support, or to Rh-assisted partial reduction of the $ZrO_2$ support.[55–59]

The $H_2$-TPR profile of $Ru/ZrO_2$ contained reduction peaks at 90 and 130 °C, and no $H_2$ consumption was observed at temperatures above 150 °C (Figure 1). Similar $H_2$-TPR profiles have been reported for $Ru/ZrO_2$ catalysts in the literature.[60–62] The first peak has been explained by the reduction of $RuO_2$ particles to metallic Ru, whereas the second peak has been proposed to involve the reduction of $RuO_2$ particles with stronger interactions with $ZrO_2$.[60–62] The $H_2$-TPR measurements therefore indicated that the Ru, Rh, Pt and Pd got reduced during the reduction treatment that was used before the activity tests, whereas part of the Ni possibly remained oxidic.

Based on the pulse chemisorption measurements, the mean metal particle size ranged between 1.9 and 2.9 nm for $Pt/ZrO_2$, $Pd/ZrO_2$, $Ru/ZrO_2$ and $Rh/ZrO_2$, whereas the dispersions varied from 38 to 61% (Table 1). Due to the uncertainty of the semi-quantitative elemental analysis, the dispersion and mean particle size were calculated based on the nominal metal loading (1 wt. %), which implies that the dispersion and mean particle size of the Pt, Pd, Ru and Rh catalysts are within the measurement accuracy of each other. Based on the $H_2$ pulse chemisorption measurement, the mean particle size (30 nm) and dispersion (4%) of $Ni/ZrO_2$ deviated from the noble metals significantly. Considering the relatively high reduction temperature (Figure 1) and the absence of Ni-related reflections in the X-ray diffractogram of the calcined $Ni/ZrO_2$ catalyst, it is possible that the low $H_2$ adsorption capacity partly was related to an incomplete reduction of Ni. A selection of representative STEM images with elemental EDS mappings is available in Figure S4 of the Supporting Information. The mean metal particle size derived from the STEM images was 2.1 nm for both $Pt/ZrO_2$ and $Rh/ZrO_2$, which is in good agreement with the pulse chemisorption results (Table S1, Supporting Information). Due to an insufficient contrast between the active metal and the support, the active metal particle size distribution could not be reliably estimated from the STEM images of the Ru, Pd and Ni catalysts.

XPS measurements were carried out for the catalysts and the bare $ZrO_2$ support to study the chemical state of the active metals and their interactions with the support. The catalyst samples were reduced ex situ in $H_2$ at 350 °C before the measurements and transferred to the equipment exposed to air. The XPS survey spectra of the samples are available in Figure S5 of the Supporting Information. Figure 2 presents

high-resolution XPS spectra of the Ni 2p (a), Pd 3d (b), Pt 4f (c), Rh 3d (d) and Ru 3d (e) regions of the $Ni/ZrO_2$, $Pd/ZrO_2$, $Pt/ZrO_2$, $Rh/ZrO_2$ and $Ru/ZrO_2$ catalysts, respectively. Table 2 summarizes the surface composition of the catalysts, and the relative amounts of active metal in reduced and oxide states.

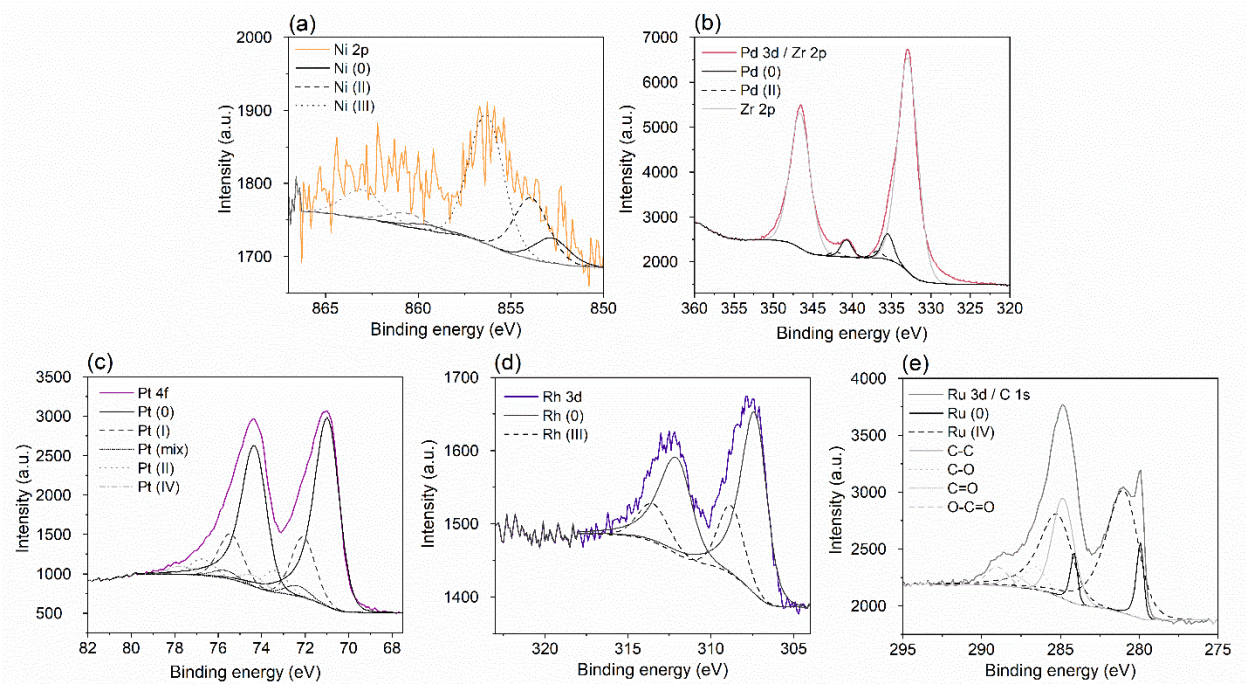


**Figure 2.** High-resolution X-ray photoelectron spectra of (a) the Ni 2p region of $Ni/ZrO_2$, (b) the Pd 3d / Zr 2p region of $Pd/ZrO_2$, (c) the Pt 4f region of $Pt/ZrO_2$, (d) the Rh 3d region of $Rh/ZrO_2$ and (e) Ru 3d / C 1s region of $Ru/ZrO_2$. The samples were reduced ex situ in $H_2$ at 350 °C before the XPS measurements and transferred to the equipment exposed to air.

**Table 2.** XPS-derived atomic surface composition and relative amounts of active metal M in reduced state M(0) and in oxidic states M(ox.)

| Catalyst[a] | Atomic surface composition[b] | | | | Oxidation states | |
|---|---|---|---|---|---|---|
| | M (at. %) | Zr (at. %) | O (at. %) | C (at. %) | M(0) (%) | M(ox.) (%) |
| $ZrO_2$ | - | 30.1 | 46.4 | 22.3 | - | - |
| $Ni/ZrO_2$ | 0.7 | 33.0 | 52.7 | 12.3 | 13.5% | 86.5% |
| $Pd/ZrO_2$ | 1.1 | 29.6 | 51.6 | 16.8 | 74.0% | 26.0% |
| $Pt/ZrO_2$ | 4.9 | 30.4 | 52.3 | 12.5 | 71.9% | 28.1% |
| $Rh/ZrO_2$ | 0.8 | 33.1 | 53.9 | 8.0 | 74.5% | 25.5% |
| $Ru/ZrO_2$ | 3.0 | 28.8 | 51.8 | 15.5 | 14.1% | 86.0% |

[a)]The samples were reduced ex situ in $H_2$ at 350 °C before the XPS measurements and transferred to the equipment in atmosphere.
[b)]The XPS measurement indicated that the $Rh/ZrO_2$ catalyst also contained 2.8 at. % potassium.

The catalysts showed differences in the surface concentration of active metal and in their oxidation states (Table 2). $Pt/ZrO_2$ and $Ru/ZrO_2$ had the highest metal surface concentration, with 4.9 at. % Pt and 3.0 at. %

Ru. The surface concentration of active metal was lower for $Pd/ZrO_2$, $Rh/ZrO_2$ and $Ni/ZrO_2$, 1.1, 0.8 and 0.7 at. %, respectively. Over 70% of the Pt, Pd and Rh was reduced, while more than 85% of the Ru and Ni was oxidic (Table 2, Figure 2). Considering the $H_2$-TPR profiles (Figure 1), where the Pt, Pd, Rh and Ru-related reduction peaks were located below 350 °C, i.e., the temperature that was used for the ex situ sample reduction, the partial surface oxidation of the noble metals may be related to the exposure to air during the sample transfer to the XPS. The oxidation states of the metals therefore likely differed from the oxidation states at reaction conditions. The high degree of oxidation of Ru nevertheless suggests that the metal got oxidized easier than the other noble metals, reflecting the intrinsic redox potential of Ru. Similar results have been reported for supported Ru catalysts elsewhere.[63] Based on $H_2$-TPR, the relatively high degree of oxidation of $Ni/ZrO_2$, i.e. the only base metal catalyst, was expected. All C 1s spectra were consistent with what would be expected for advantageous carbon, with roughly 60 % or more of the intensity in a main C-C component together with three minor components at approximately 286.5 eV, 288.0 eV, and 289.2 eV, corresponding to different states of bonding with oxygen.

The catalysts exhibited some differences in the state of the $ZrO_2$ support and in the Zr 3d and O 1s binding energies, potentially reflecting electron transfer between the active metals and the support. Notably, the Zr 3d and O 1s binding energies on $Rh/ZrO_2$ were approximately 0.3 eV lower compared to the bare $ZrO_2$ support, which may indicate electron transfer from Rh to the support. Table S2 of the Supporting Information displays the oxidation states of $ZrO_2$, while Figures S6a and S6b of the Supporting Information present the high resolution XPS spectra of the Zr 3d and O 1s regions, respectively.

Basic and acid site characterization were carried out via $CO_2$-TPD measurements and FTIR spectroscopy of pyridine adsorption, respectively. Figure 3a displays the $CO_2$-TPD profiles, while the transmission FTIR spectra of the pyridine-saturated catalysts (170 °C) with the spectra of the clean samples and the background subtracted are presented in Figure 3b.

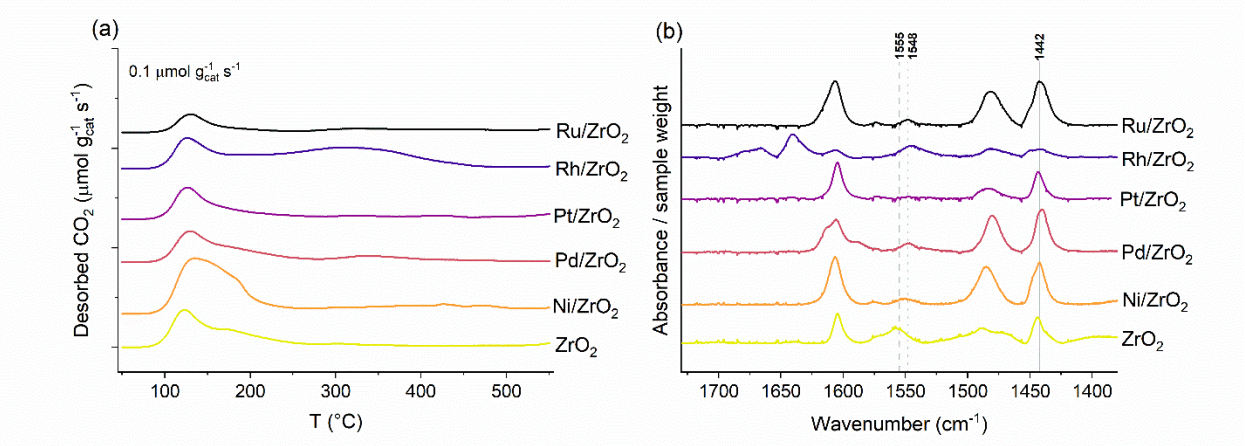


**Figure 3.** Analysis of the calcined catalysts via (a) $CO_2$-TPD and (b) transmission FTIR of adsorbed pyridine. The spectra of the clean samples and the background have been subtracted from the spectra of the pyridine-saturated samples. The vertical lines indicate the vibration bands characteristic for pyridine adsorbed on Lewis acid sites (1442 $cm^{-1}$) and Brønsted acid sites (1548 and 1555 $cm^{-1}$). The data has been vertically shifted for clarity.

Based on the $CO_2$ desorption profiles (Figure 3a), the $CO_2$ adsorption strength and $CO_2$ adsorption capacity were similar for the bare $ZrO_2$ support (36 µmol/g), Pd/$ZrO_2$ (36 µmol/g) and Pt/$ZrO_2$ (30 µmol/g). This suggests that the adsorption of $CO_2$ on Pt/$ZrO_2$ and Pd/$ZrO_2$ mainly occurred on the support. The $CO_2$ desorption profiles contained a broad peak with maximum intensity at 120 °C and a shoulder at approximately 150 °C. The $CO_2$ may have adsorbed as bicarbonate species on Brønsted basic OH groups, as monodentate carbonate species on Lewis basic $O^{2-}$ centers and as bidentate carbonate species on Lewis acid–base ($Zr^{4+}$-$O^{2-}$) pairs.[48,64] The bidentate carbonate species likely accounted for the shoulder at 150 °C.[64] The $CO_2$ adsorption capacity of the Ru/$ZrO_2$ catalyst (16 µmol/g) was less than half compared to the bare $ZrO_2$ support, and the desorption peak did not contain the shoulder at 150 °C, indicating that the impregnation of Ru suppressed the amount of the strongest basic sites or acid–basic site pairs of the $ZrO_2$ support.

The $CO_2$ adsorption capacity of Ni/$ZrO_2$ (63 µmol/g) and Rh/$ZrO_2$ (66 µmol/g) was approximately 30 µmol/g higher compared to the bare $ZrO_2$ support, which suggests that the $CO_2$ partly adsorbed on the active metals or the interface between the active metal and the support (Table 1). The $CO_2$ desorption peak of Ni/$ZrO_2$ was in a similar temperature range as for the $ZrO_2$ support, but a relatively larger share of the $CO_2$ desorption occurred above 150 °C (Figure 3a). The $CO_2$ desorption profile of Rh/$ZrO_2$ contained both the peak around 120 °C, related to $CO_2$ adsorbed on $ZrO_2$, and a broad peak which reached maximum

intensity around 300 °C. The high-temperature peak may be related to $CO_2$ that was adsorbed on Rh, but might also be related to the K on the catalyst surface (Table 2).[65] Based on the desorption temperature, the basic sites on the $Rh/ZrO_2$ catalyst were considerably stronger compared to the other catalysts.

As described previously, Lewis and Brønsted acid sites are mechanistically involved in several reactions of the amide hydrotreatment reaction network.[27] The total acid site concentration was 80 µmol/g or lower for the studied catalysts, and the vibration bands characteristic for pyridine adsorbed on Lewis acid sites and Brønsted acid sites were located at 1442 $cm^{-1}$ and 1548 $cm^{-1}$, respectively (Figure 3b). Therefore, the $ZrO_2$-supported catalysts had a relatively low acid site concentration, and the acid sites were weak compared to catalysts supported on other inorganic oxides, such as ɣ-$Al_2O_3$, $SiO_2$-$Al_2O_3$ and $TiO_2$.[66,67] The bare $ZrO_2$ support had 40 µmol/g Brønsted acid sites and 30 µmol/g Lewis acid sites. The impregnation of Pt, Pd, Ni and Ru suppressed the Brønsted acid site concentration to less than 20 µmol/g, whereas the Lewis acid site concentration was unaffected for $Pt/ZrO_2$ and increased to 60-70 µmol/g for $Pd/ZrO_2$, $Ni/ZrO_2$, and $Ru/ZrO_2$. The differences in the acidity of these catalysts fell within the measurement uncertainty and are not expected to have a significant influence on the catalytic activity.

$Rh/ZrO_2$ was the only catalyst where the concentration of Brønsted acid sites (40 µmol/g) exceeded the concentration of Lewis acid sites (20 µmol/g). It is possible that the K on the catalyst surface (Table 2) suppressed the Lewis acidity of the catalyst.[68] The acid–base properties of $Rh/ZrO_2$ therefore deviated from the other catalysts.

3.2 Catalytic Hydrotreatment of *n*-Hexadecanamide. Hydrotreatment experiments were performed at 300 °C and 80 bar $H_2$, using *n*-hexadecanamide (C16 amide) as the model compound and a reaction time of 60 min. The main products of the C16 amide hydrotreatment experiments were *n*-pentadecane (C15 paraffin), *n*-hexadecane (C16 paraffin), *n*-hexadecanal (C16 aldehyde), 1-hexadecylamine (C16 amine), 1-hexadecanol (C16 alcohol), *n*-hexadecanonitrile (C16 nitrile), palmitic acid (C16 acid), dipentadecyl ketone (31 ketone), *n*-hexadecyl hexadecylamine (C32 amine), palmityl palmitate (C32 ester) and *n*-hexadecyl hexadecanamide (C32 amide). The product distribution, conversion, nitrogen removal and oxygen removal of the C16 amide hydrotreatment experiments at a reaction time of 60 min are shown in Figure 4. The nitrogen removal is based on the total nitrogen content analysis, while the oxygen removal was derived from the GC data. Figure S7 of the Supporting Information shows the product distribution of the catalysts at a similar conversion level.

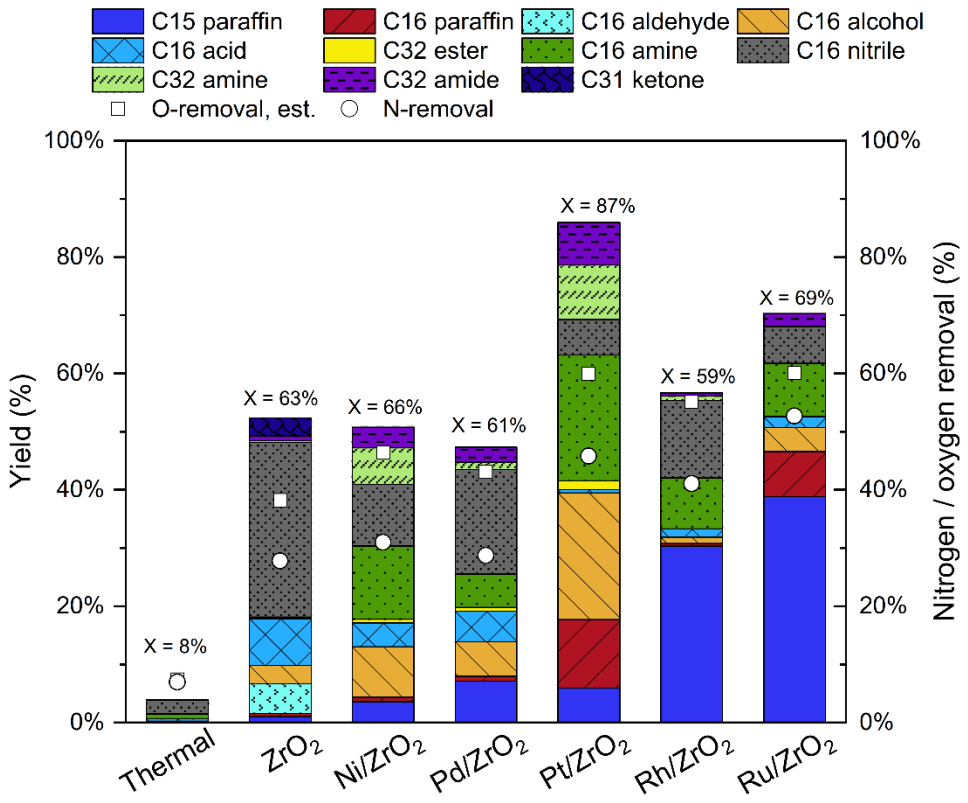


**Figure 4.** Product distribution, conversion, nitrogen removal and oxygen removal in the hydrotreatment of the C16 amide. The experiments were carried out at 300 °C and 80 bar $H_2$ for 60 min, stirring 600 rpm and using an initial nitrogen content of 100 ppm. The nitrogen removal is based on the total nitrogen content analysis, while the oxygen removal was derived from the product distribution.

The studied catalysts and the bare $ZrO_2$ support exhibited activity for the conversion of the C16 amide (Figure 4). The nitrogen removal of the 60 min reference experiments increased in the order of $ZrO_2$ (28%), Pd (29%), Ni (31%) << Rh (41%) < Pt (46%) < Ru (53%). Based on the product distribution, the oxygen removal increased in the order of $ZrO_2$ < Pd < Ni << Rh < Pt ≈ Ru, reaching approximately 60% on the most active catalysts. The oxygen removal exceeded the nitrogen removal on the studied catalysts. Scheme 1 displays a proposed reaction network for the hydrotreatment of the C16 amide. The reaction network has been modified from a previous work by Verkama et al.,[28] by the addition of the reaction pathway for the conversion of the C16 amine to the C15 paraffin.

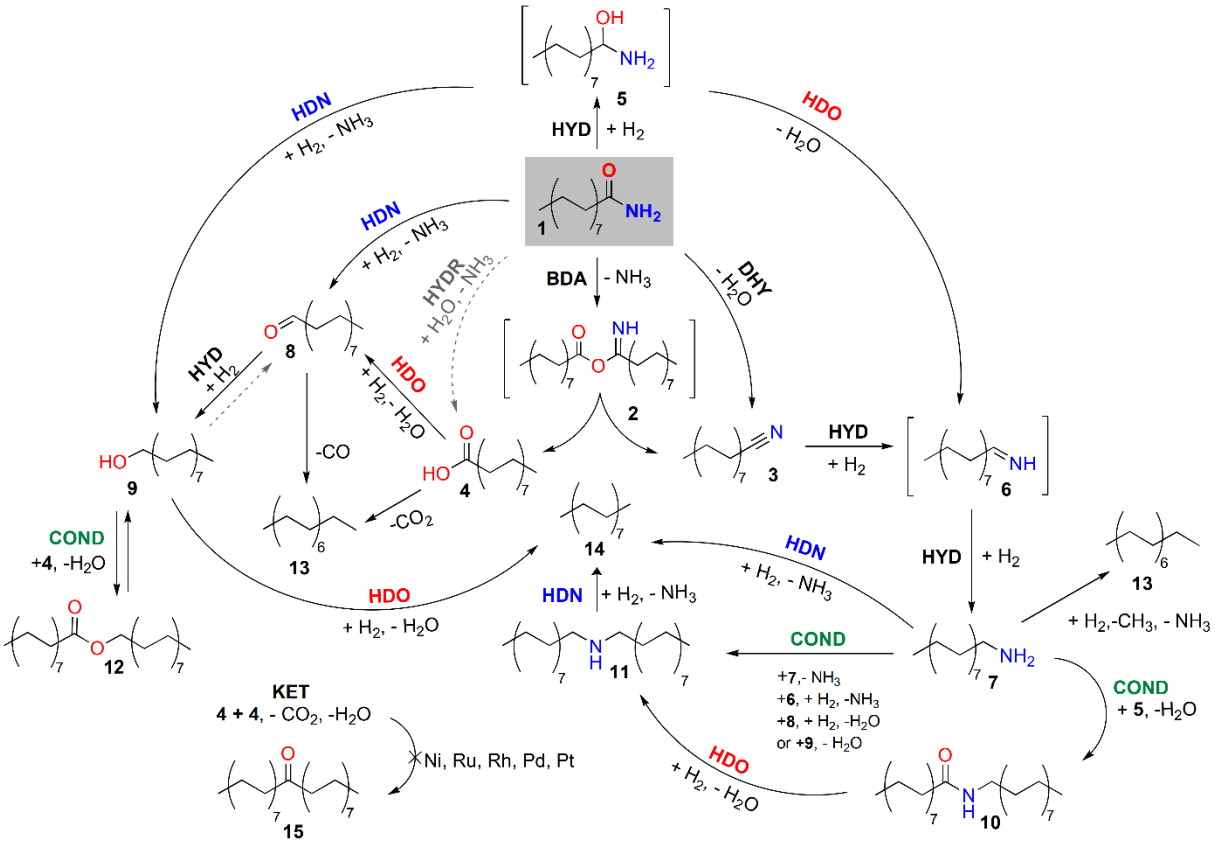


**Scheme 1.** Proposed reaction network for the hydrotreatment of *n*-hexadecanamide, including the reaction network for the hydrotreatment of 1-hexadecylamine. The following compounds have been indicated: (1) C16 amide, (2) C32 isoimide, (3) C16 nitrile, (4) C16 acid, (5) C16 hemiaminal, (6) C16 imine, (7) C16 amine, (8) C16 aldehyde, (9) C16 alcohol, (10) C32 amide, (11) C32 amine, (12) C32 ester, (13) C15 paraffin, (14) C16 paraffin and (15) C31 ketone. The following reactions are named: bimolecular deammoniation (BDA), condensation (COND), direct dehydration (DHY), hydrodenitrogenation (HDN), hydrodeoxygenation (HDO), hydrogenation (HYD) and hydrolysis (HYDR). The disproportionation of the C16 amine is included in the condensation reactions. The bimolecular ketonization of the C16 acid (KET) was only observed on the bare support. Note that the C15 paraffin (13) is indicated in two locations. The reaction network has been adapted and extended from Reference 27 with permission from the Royal Society of Chemistry.

Hydrotreatment experiments with different batch residence times were conducted for the two most active catalysts, $Pt/ZrO_2$ and $Ru/ZrO_2$. Figure 5 displays the product distribution of $Pt/ZrO_2$ (a) and $Ru/ZrO_2$ (b) in the hydrotreatment of the C16 amide, as a function of batch residence time. The experiments were carried out at 300 °C and 80 bar $H_2$, using 20 mg catalyst and an initial nitrogen content of 100 ppm. The 60 min reference experiments of Figure 4 correspond to the batch residence time 0.37 $g_{cat}h/g_{amide}$. The product distribution of the different catalysts is discussed in the following paragraphs. The product

distribution of $Pt/ZrO_2$ at batch residence times below 0.5 $g_{cat}h/g_{amide}$ has been magnified in Figure S8 of the Supporting Information.

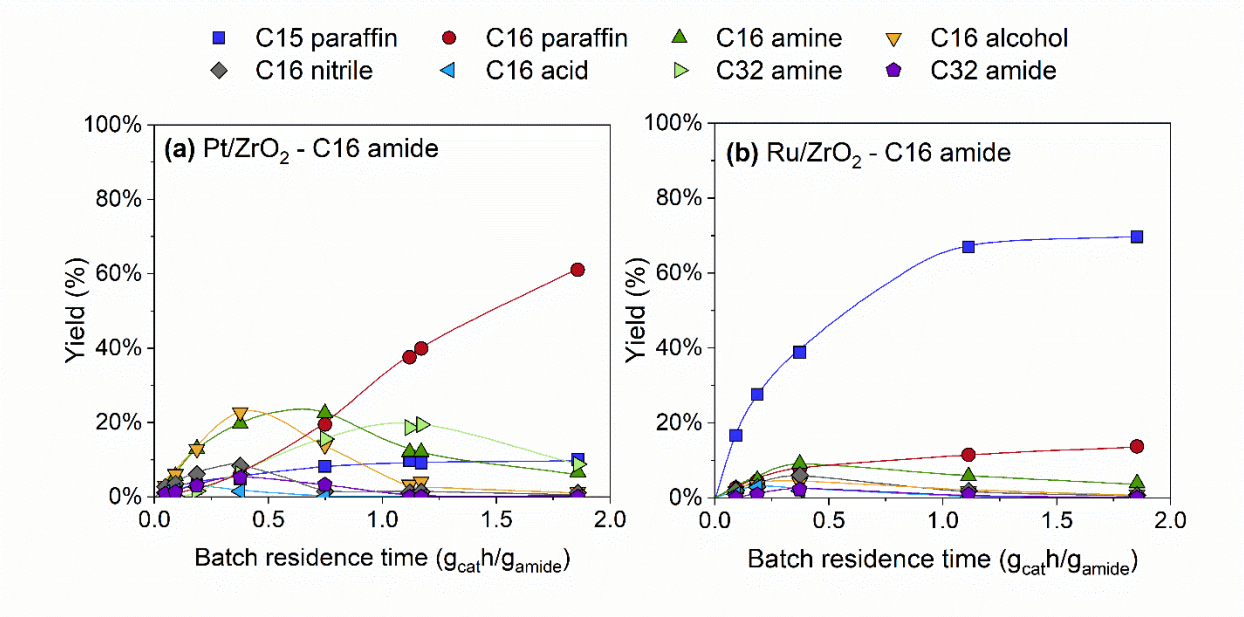


**Figure 5.** Product distribution as a function of batch residence time for (a) $Pt/ZrO_2$ and (b) $Ru/ZrO_2$ in the hydrotreatment of the C16 amide. The experiments were carried out at 300 °C, 80 bar $H_2$, using 20 mg of catalyst and an initial nitrogen content of 100 ppm. The trendlines have been added to guide the eye.

The bare $ZrO_2$ support was active for the conversion of the C16 amide to the C16 nitrile and C16 acid (Figure 4) via bimolecular deammoniation (BDA, Scheme 1). The reaction was likely Lewis acid site catalyzed.[27] The reaction pathway has been described by Davidson and Karten.[69] The C16 amide may additionally have been converted to the C16 nitrile via dehydration and to the C16 acid via hydrolysis.[70] In line with literature, the conversion of the C16 amide via BDA and dehydration additionally occurred thermally, but with an approximately 90% lower activity compared to the $ZrO_2$ support.[69] Furthermore, the bare $ZrO_2$ support was active for the conversion of the C16 acid to the C16 aldehyde and the bimolecular ketonization of the C16 acid to the C31 ketone.[71–73] The oxygen vacancies on $ZrO_2$ have been suggested to catalyze these reactions.[71–73] A part of the C16 aldehyde was further converted to the C16 alcohol. The C31 ketone and the reactive C16 aldehyde were not detected in the product samples of the metal catalysts. The activity of the $ZrO_2$ support in the hydrotreatment of the C16 amide has been discussed in detail in a previous work by Verkama et al.[27]

In line with a previous work by Verkama et al.,[27] the product distribution and conversion of the C16 amide on the different catalysts (Figure 4) indicated that the initial C16 amide conversion route was significantly influenced by the $ZrO_2$ support (Scheme 1). This was particularly evident in the case of $Pd/ZrO_2$ and $Ni/ZrO_2$, which exhibited a similar activity and selectivity as the bare $ZrO_2$ support in the hydrotreatment of the C16 amide. Meanwhile, the active metal was decisive for the activity and pathway selectivity for the conversion of the intermediate products via the hydrogenation and hydrogenolysis routes.

The main difference between the bare support and $Pd/ZrO_2$ was that $Pd/ZrO_2$ showed activity towards decarbonylation of the C16 aldehyde and/or decarboxylation of the C16 acid, resulting in a 7% C15 paraffin yield, and produced C16 alcohol and C16 amine through hydrogenation of the C16 aldehyde and C16 nitrile, respectively (Figure 4). The C16 amine and C16 alcohol yields were both 6% on $Pd/ZrO_2$, whereas only 1% of the C16 paraffin was formed. The amounts of CO and $CO_2$ were below the detection limit of the gas phase analysis, due to the low initial concentration of the model compound.

$Ni/ZrO_2$ showed a higher hydrogenation activity than $Pd/ZrO_2$, as indicated by the C16 amine and C16 alcohol yields of 13% and 9%, respectively (Figure 4). Similarly to $Pd/ZrO_2$, $Ni/ZrO_2$ only gave 1% of the C16 paraffin, but produced less C15 paraffin (4%). $Ni/ZrO_2$ produced more C32 amine compared to $Pd/ZrO_2$ (6% vs 1%), whereas the C32 amide yields were similar (3-4%). The molar carbon balance closure of the C16 amide experiments on $Pd/ZrO_2$ and $Ni/ZrO_2$ (~85%) was lower than for the other catalysts (>90%), potentially hinting towards the formation of heavy, nonvolatile products that could not be detected by GC-FID. For example, the formation of trihexadecylamine (C48 amine) may have occurred.[74–77] The low activity of the Ni catalyst may have been related to the relatively low number of surface Ni sites (Table *1*). Considering the low price of Ni compared to noble metals, it could be viable to increase the Ni loading in order to increase the reaction rate.[23,78,79]

The activity of $Pt/ZrO_2$ markedly exceeded the activity of $Ni/ZrO_2$ and $Pd/ZrO_2$, but the product distribution shared some similarities (see Figure S7 of the Supporting information for the product distribution at similar conversion levels). $Pt/ZrO_2$ provided the highest conversion (87%) out of the studied catalysts in the hydrotreatment of the C16 amide (Figure 4). The hydrogenation activity of $Pt/ZrO_2$ was superior to the other catalysts, as suggested by the relatively low C16 nitrile yield (6%) in the 60 min reference experiment, and high yields of the C16 amine (22%), C16 alcohol (22%) and C16 paraffin (12%). $Pt/ZrO_2$

was, consequently, the only catalyst that was more selective towards the C16 paraffin than the C15 paraffin in the tested conditions (Figure 5a).

The product sample of the 60 min reference experiment on $Pt/ZrO_2$ (Figure 4) additionally contained the C32 amine (9%), the C32 amide (7%) and the C32 ester (2%), which were converted to the C16 paraffin at higher batch residence times (Scheme 1, Figure 5a). The condensation reactions and competitive HDN and HDO of the C16 amine and C16 alcohol characterized the reaction network of $Pt/ZrO_2$, as discussed in detail previously.[27,28] Up to 10% of the C15 paraffin was formed via decarboxylation and decarbonylation routes on $Pt/ZrO_2$, but based on the batch residence time series (Figure 5a), the C–C bond hydrogenolysis of the C16 alcohol to the C15 paraffin was not favored. The pathway may have been more prominent on the metals which bind $CH_x$ species stronger, such as Ru, Rh and Ni, as the selectivity between the C–O and C–C bond hydrogenolysis of alcohols has been found to depend on the relative ability of the metal to activate $CH_x$ species.[33,34,80–82] Lewis acid sites on the support (Figure 3b) and high $H_2$ pressures can inhibit decarbonylation reactions, which may have further contributed to why the conversion of the C16 alcohol to the C15 paraffin was not favorable on $Pt/ZrO_2$.[5,82]

The enhanced C–O bond hydrogenolysis selectivity of Pt compared to Pd has been reported before and can be attributed to the metal properties, as Pd favors alkyl chain adsorption, while Pt may preferentially interact with carbonyl and hydroxyl functionalities.[5,80,83–86] Stronger interactions between the active metal and the carbonyl group of the C16 amide may likewise explain why the C16 amide conversion was higher on $Pt/ZrO_2$ than on $Pd/ZrO_2$. However, a contribution of the differences in the surface composition and possibly the dispersion of the catalysts cannot be entirely excluded (Table 1, Table 2).

The product distribution of $Ru/ZrO_2$ and $Rh/ZrO_2$ shared similarities with each other and deviated from $Ni/ZrO_2$, $Pd/ZrO_2$ and $Pt/ZrO_2$. The Ru and Rh catalysts produced the highest paraffin yields in the hydrotreatment of the C16 amide (Figure 4). Both catalysts readily produced the C15 paraffin, with yields of 39% and 30% for $Ru/ZrO_2$ and $Rh/ZrO_2$, respectively. With a conversion of 69%, $Ru/ZrO_2$ was more active than $Rh/ZrO_2$, which converted 59% of the C16 amide.

The product sample of the C16 amide hydrotreatment experiment on $Rh/ZrO_2$ did not contain C16 paraffin, and the total yield of the oxygen-containing intermediate products was only 3% (Figure 4). Together with the C15 paraffin yield, this highlights that $Rh/ZrO_2$ was highly active and selective for oxygen

removal via C–C bond cleavage routes (Scheme 1). The enhanced Brønsted acid site concentration on $Rh/ZrO_2$ (Figure 3b) was thus not reflected in the product distribution, as Brønsted acid sites promote C–O and C–N hydrogenolysis routes.[5,87] It is possible that the strong Lewis basic sites on the Rh catalyst (Figure 3a) facilitated the adsorption of carbonyl compounds, and thus enhanced the deoxygenation activity.[5,88] Only traces of the C32 condensation products were found in the product sample of $Rh/ZrO_2$.

The C15 paraffin dominated the product distribution of $Ru/ZrO_2$ in the hydrotreatment of the C16 amide, but some C16 paraffin was formed additionally (Figure 5b). The C16 intermediates and the C32 condensation products were not formed on $Ru/ZrO_2$ to the same extent as on $Pt/ZrO_2$ (Figure 5a). Therefore, in sharp contrast to $Pt/ZrO_2$, the HDN and HDO of the C16 amide on $Ru/ZrO_2$ appeared to occur simultaneously or consecutively without significant desorption of the intermediates between the HDN and HDO steps (Figure 5b). Methane was found in the qualitative analysis of the gas phase sample of both $Ru/ZrO_2$ and $Rh/ZrO_2$, indicating methanation of the C1 compounds that were formed in parallel with the C15 paraffin.[89,90] The formation of $C_{n-1}$ paraffins out of $C_n$ fatty acids has been proposed to occur through the splitting of a formic acid species on supported Pd catalysts.[84,91] Similarly, the formation of the C15 paraffin through scission of a formamide type species from the C16 amide might be a possibility for $Ru/ZrO_2$ and $Rh/ZrO_2$. Due to the high deoxygenation activity of the catalysts and the thermal instability of formamide in the studied conditions, the favored C–C bond cleavage route could not be deduced from the activity test data.

The C–C bond cleavage activity of supported Ru and Rh catalysts has been demonstrated in the hydrotreatment of vegetable oils, fatty acids and alcohols,[23,79,80] but to our knowledge, the selective C–C bond cleavage of fatty amides has not been reported before. Furthermore, with most amine hydrotreatment studies focusing on methylamine, information on the preference between C–C and C–N bond cleavage routes on reduced metal catalysts is limited. The hydrotreatment of the C16 amine was therefore studied separately.

3.3 Catalytic Hydrotreatment of 1-Hexadecylamine. Hydrotreatment experiments were carried out for the catalysts using the C16 amine as a model compound, in order to evaluate the HDN activity and the preference for C–N and C–C bond cleavage routes without the interference of simultaneous HDO. The experiments were carried out at 300 °C and 80 bar $H_2$, using a reaction time of 60 min. The products of the C16 amine hydrotreatment experiments were the C15 paraffin, the C16

paraffin, the C32 amine and traces of the C16 nitrile and the C16 alcohol. The product samples additionally contained isopropyl hexadecylamine (C19 amine), which likely was formed via a reaction between the C16 amine and acetone residues in the system (acetone was used to wash the reactor lines between the experiments). The C19 amine is not considered to be a true part of the C16 amine HDN reaction network and is therefore not discussed further. The product distribution, conversion and nitrogen removal of the C16 amine experiments is shown in Figure 6. The reaction network for the hydrotreatment of the C16 amine is a part of the reaction network of the C16 amide (Scheme 1).

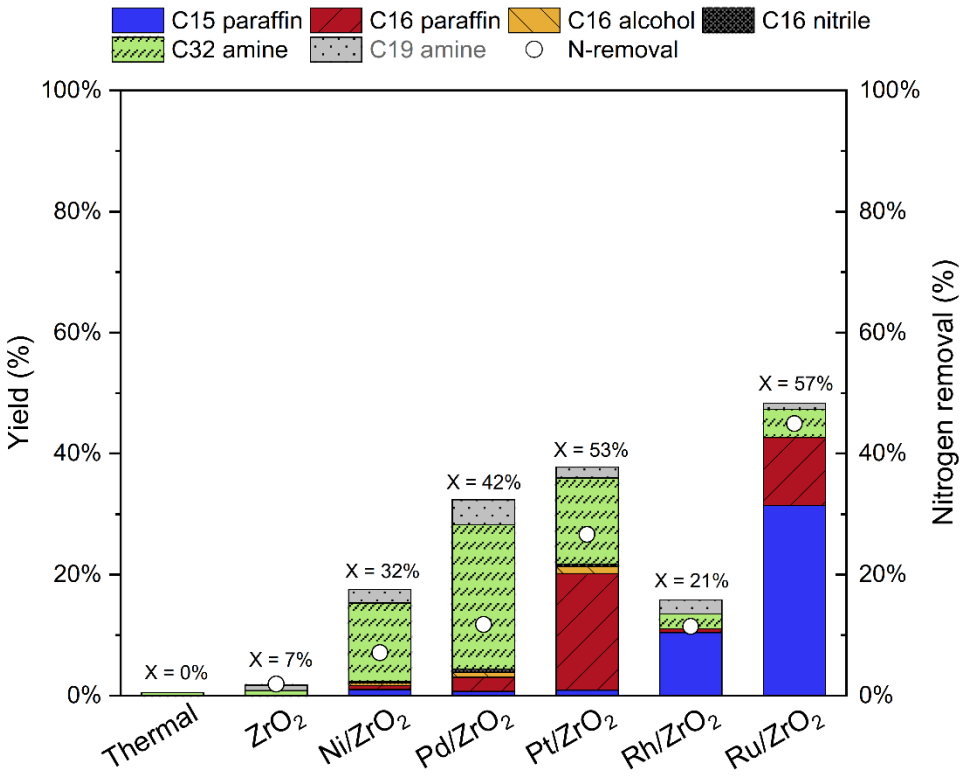


**Figure 6.** Product distribution, conversion and nitrogen removal in the hydrotreatment of the C16 amine. The experiments were carried out at 300 °C and 80 bar $H_2$ for 60 min, stirring 600 rpm and using an initial nitrogen content of 100 ppm. The nitrogen removal is based on the total nitrogen content analysis.

The nitrogen removal in the 60 min C16 amine hydrotreatment experiments (Figure 6) increased in the order of $ZrO_2$ (1%) < Ni (7%) < Rh (11%), Pd (12%) << Pt (27%) << Ru (45%). A partly different ranking by HDN activity was thus obtained, and the variation in the nitrogen removal was considerably larger compared to the C16 amide hydrotreatment experiments (Figure 4) where the difference between the nitrogen removal of the most active and least active material was 25 percentage points. While all studied

catalysts showed a lower activity in the hydrotreatment of the C16 amine than in the hydrotreatment of the C16 amide, the difference was particularly pronounced on $Rh/ZrO_2$, which removed 30 percentage points less nitrogen in the C16 amine experiment.

Batch residence time series experiments were carried out on the two most active catalysts, $Pt/ZrO_2$ and $Ru/ZrO_2$. Figure 7 displays the product distribution of $Pt/ZrO_2$ (a) and $Ru/ZrO_2$ (b) in the hydrotreatment of the C16 amine as a function of batch residence time. The experiments were performed at 300 °C and 80 bar $H_2$, using 20 mg catalyst and an initial nitrogen content of 100 ppm. The 60 min reference experiments shown in Figure 6 correspond to the batch residence time 0.39 $g_{cat}h/g_{amine}$. The following paragraphs discuss the activity and product distribution of the C16 amine hydrotreatment experiments on the catalysts.

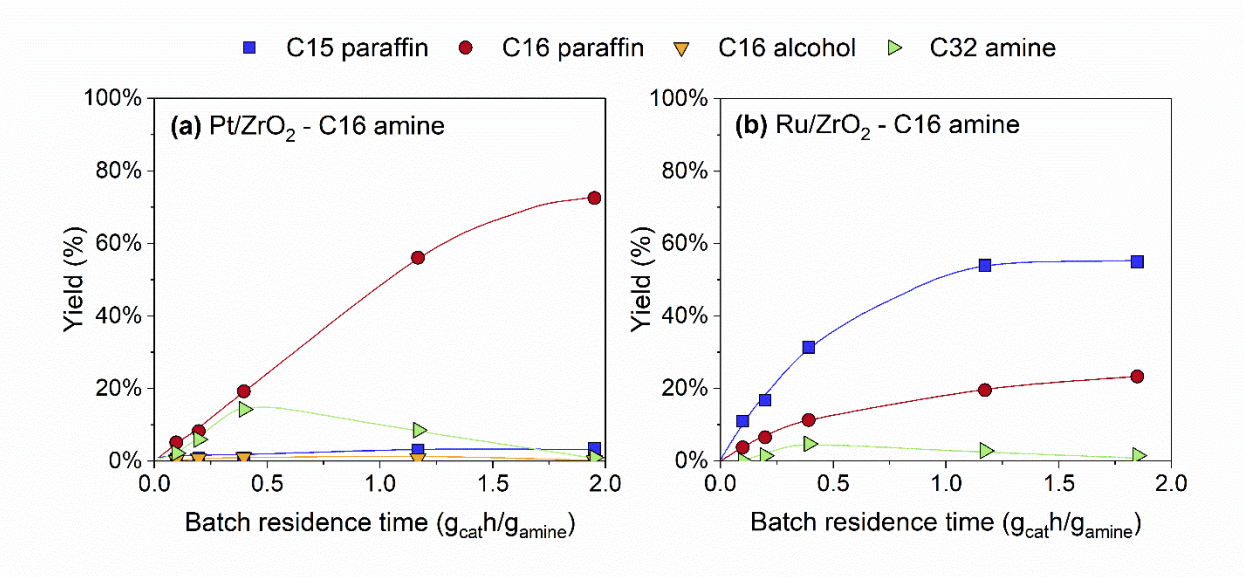


**Figure 7.** Product distribution as a function of batch residence time for (a) $Pt/ZrO_2$ and (b) $Ru/ZrO_2$ in the hydrotreatment of the C16 amine. The experiments were carried out at 300 °C, 80 bar $H_2$, using 20 mg of catalyst and an initial nitrogen content of 100 ppm. The trendlines have been added to guide the eye.

In contrast to the C16 amide hydrotreatment experiment (Figure 4), the $ZrO_2$ support showed a negligible nitrogen removal in the HDN of the C16 amine (Figure 6). The sites of $ZrO_2$ were therefore unable to catalyze reactions of the C16 amine in the tested conditions, which accounts for the lower conversion and nitrogen removal of the metal catalysts compared to the C16 amide experiments, where the support alone

removed 28% nitrogen via BDA (Scheme 1). No thermal activity was recorded in the hydrotreatment of the C16 amine.

The C32 amine dominated the product distribution of $Ni/ZrO_2$ and $Pd/ZrO_2$ in the hydrotreatment of the C16 amine, with yields of 13% and 24%, respectively (Figure 6). The catalysts were therefore mainly active for the disproportionation of the C16 amine (Scheme 1).[25] The total paraffin yield of the C16 amine experiments was less than 2% on $Ni/ZrO_2$ and 3% on $Pd/ZrO_2$, with Ni favoring the C15 paraffin and Pd favoring the C16 paraffin. The majority of the paraffins that were formed in the C16 amide experiments over $Ni/ZrO_2$ and $Pd/ZrO_2$ (Figure 4) therefore appeared to originate from the C16 acid, the C16 aldehyde or the C16 alcohol.

As with the C16 amide experiments (Figure 4), $Pt/ZrO_2$ exhibited the highest C16 paraffin yield (19%) out of the tested catalysts in the C16 amine hydrotreatment experiments (Figure 6). The C16 paraffin could be formed as a primary product in the hydrotreatment of the C16 amine on $Pt/ZrO_2$, which initially was reflected in higher C16 paraffin yields compared to a similar batch residence time with the C16 amide, despite a lower model compound conversion. The C16 to C15 paraffin ratio at the highest studied batch residence time was significantly higher in the hydrotreatment of the C16 amine (21.0 mol/mol, Figure 7a) compared to the hydrotreatment of the C16 amide (6.1 mol/mol, Figure 5a). The C–C bond cleavage of the C16 amine to the C15 paraffin did therefore not significantly occur on $Pt/ZrO_2$. This indicates that the C15 paraffin that was formed on $Pt/ZrO_2$ in the C16 amide experiments originated from decarbonylation and decarboxylation pathways (Scheme 1). The C16 paraffin and C32 amine yields were similar until batch residence time 0.39 $g_{cat}h/g_{amine}$.

Similar results have been reported previously for the activity of Pt and Pd in HDN. In their computational study, Almithn and Hibbis[33] found Pt to be more active than Pd for the C–N bond hydrogenolysis of methylamine, while Meitzner et al.[25] found that Pd was more selective for the disproportionation of methylamine to dimethylamine than Pt. In the 60 min C16 amine hydrotreatment experiments on $Pd/ZrO_2$ and $Pt/ZrO_2$, we obtained C32 amine to C16 paraffin ratios of 5 mol/mol and 0.4 mol/mol, respectively (Figure 6), which considering the higher reaction temperature and conversion level, aligns with the observations by Meitzner et al.[25] On the other hand, Ni has been predicted to be more active in C–N bond hydrogenolysis than both Pd and Pt.[33] It is possible that the low HDN activity of $Ni/ZrO_2$ was due to the poor Ni dispersion (Table 1) or incomplete reduction of Ni (Figure 1).

Interestingly, up to 2% of the C16 alcohol was found in the product samples of the C16 amine hydrotreatment experiments on $Pt/ZrO_2$ and $Pd/ZrO_2$ (Figure 6). The compound may have been formed using oxygen from the $ZrO_2$ surface. In a previous work by Verkama et al.,[28] the formation of alcohols from amines was observed on $Pt/ZrO_2$ in similar reaction conditions. Therefore, the conversion of the C16 amine to the C16 alcohol, and vice versa, likely occurred in the C16 amide experiments as well.[92]

The C15 paraffin was obtained as the main product in the C16 amine hydrotreatment experiments on $Ru/ZrO_2$ and $Rh/ZrO_2$, with yields of 31% and 10%, respectively (Figure 6). This confirms that $Ru/ZrO_2$ and $Rh/ZrO_2$ are active for the C–C bond cleavage of primary alkyl amines. Methane was found in the qualitative gas-phase analysis, but the absence of *n*-tetradecane (C14 paraffin) and other shorter chain paraffins in the product samples indicate that the C–C bond cleavage of the C16 amine to the C15 paraffin is more likely than cracking of the C16 paraffin to the C15 paraffin and methane. This is also supported by the batch residence time series experiments (Figure 5, Figure 7), where the paraffin yields did not decay over time. Di et al.[80] similarly found that $Ru/TiO_2$ catalyzed both the C–C and C–N bond hydrogenolysis of the C16 amine, and obtained methane as the exclusive carbon-containing gaseous product. The C32 amine yields were below 5% on both $Ru/ZrO_2$ and $Rh/ZrO_2$, in contrast to $Pt/ZrO_2$, $Pd/ZrO_2$ and $Ni/ZrO_2$, which favored the formation of the C32 amine.

$Ru/ZrO_2$ produced a C16 paraffin yield of 11% in the C16 amine experiment (Figure 6), which is higher than the C16 paraffin yield in the C16 amide experiments (Figure 4). This was also reflected in the batch residence time series experiments on $Ru/ZrO_2$, where C16 to C15 paraffin ratios of 0.4 mol/mol and 0.2 mol/mol were obtained at the highest batch residence time points for the C16 amine (Figure 7b) and C16 amide (Figure 5b), respectively. $Ru/ZrO_2$ was therefore less selective for the C-C bond cleavage of the C16 amine than for the C-C bond cleavage of the oxygen-containing compounds in the C16 amide reaction network (Scheme 1).

The product sample of the C16 amine hydrotreatment experiment on $Rh/ZrO_2$ did not contain C16 paraffin, which implies that $Rh/ZrO_2$ was the most selective catalyst for the C–C bond cleavage routes, regardless of its relatively low activity. Rh has been reported to exhibit a high activity for the C–N bond hydrogenolysis of methylamine to methane, which makes the low C16 amine conversion and complete lack of C16 paraffin in the C16 amine HDN experiments on $Rh/ZrO_2$ surprising, particularly considering

that the C–C bond dissociation energy is higher than the C–N bond dissociation energy.[25,29,33] Preferential interaction between the Rh sites and the alkyl chain, preventing the adsorption of the C16 amine in a favorable mode for C-N bond hydrogenolysis and stabilizing the transition states for the C–C bond cleavage route, might explain the selectivity of $Rh/ZrO_2$ in the hydrotreatment of the C16 amine. It is also possible that the relatively low concentration of Lewis acid sites (Figure 3b), strong basic sites (Figure 3a) and electronic interactions between Rh and the support (Table S2, Supporting Information) influenced the catalytic properties of $Rh/ZrO_2$ in this context.

The mechanism for the formation of the C15 paraffin, the C16 paraffin and the C32 amine from the C16 amine cannot be confirmed from the experimental data, but it is likely that the reactions were initiated by the dissociative adsorption of the C16 amine as a hydrogen-deficient surface intermediate $C_{15}H_{31}CH_xNH_y$, and followed by a sequence of dehydrogenation, hydrogenation and C–C or C–N bond cleavage steps on the metal sites.[25,29–34,81,93–95] The active metal influences the adsorption strength, preferred adsorption mode and transition states in the reaction mechanism, which can explain the differences in the activity and selectivity towards the different reaction pathways.[25,29–34,81,93–95]

The activity of the metals of the groups 8-11 has been found to decrease from left to right in the periodic table, both in the case of C–C and C–N bond hydrogenolysis.[25,29,33,96] While the amine group affects the reactivity of the adjacent C–C bond, the periodic trend for the activity towards C–C bond cleavage is reflected in the product distribution of the C16 amine experiments (Figure 6).[33,96,97] In contrast, the periodic trend for the activity towards C–N bond cleavage only holds in the case of $Pt/ZrO_2$ and $Pd/ZrO_2$.[25,33] This could indicate that the relative ability of the metals to activate $CH_x$ species influenced the preference between C–C and C–N bond cleavage, similarly to what has been found in the hydrotreatment of alcohols.[82]

3.4 Comparison of the model compounds. Figure 8 presents the heteroatom removal in the hydrotreatment of the C16 amide and the C16 amine as a function of conversion for the catalysts and the $ZrO_2$ support. The data is from the 60 min reference experiments at 300 °C and 80 bar $H_2$ (Figure 4, Figure 6).

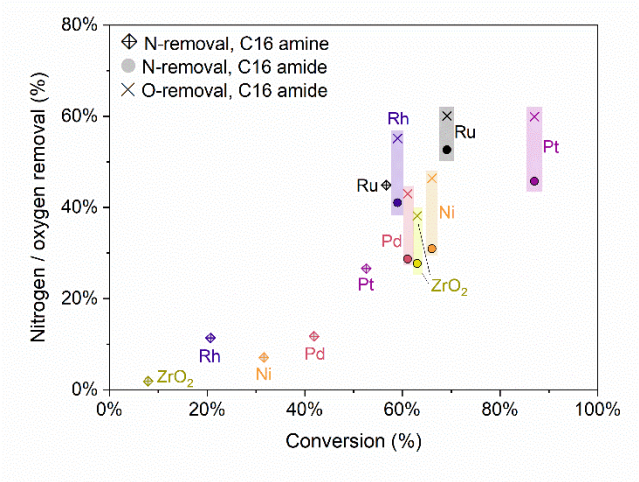


**Figure 8.** Heteroatom removal as a function of conversion in the hydrotreatment of the C16 amide and the C16 amine on the catalysts and the bare $ZrO_2$ support. Reaction conditions: 300 °C, 80 bar $H_2$, 60 min, 100 ppm initial N content, 20 mg catalyst.

The catalysts showed a higher conversion and nitrogen removal in the C16 amide hydrotreatment experiments than in the C16 amine hydrotreatment experiments (Figure 8), which can be explained by the activity of the $ZrO_2$ support for the conversion of the C16 amide via BDA (Scheme 1). Ru/$ZrO_2$ and Pt/$ZrO_2$ were the most active catalysts in terms of conversion and heteroatom removal in the hydrotreatment of both model compounds, but the order of activity varied for the other catalysts. While the initial conversion of the C16 amide to oxygen-containing and nitrogen-containing intermediate products proceeded efficiently, the further HDN of the nitrogen-containing intermediates was inhibited by the competitive HDO of the oxygen-containing intermediates.[28] The preference for HDO was reflected in a higher oxygen removal than nitrogen removal on the catalysts (Figure 4), and could also be observed from the product distribution of the batch residence time series experiments (Figure 5).

The interference of HDO may explain why the ranking of the catalysts by HDN activity differed in the C16 amide experiments and the C16 amine experiments (Figure 8). For example, the nitrogen removal of Pd/$ZrO_2$ was similar to the nitrogen removal of the bare $ZrO_2$ in the hydrotreatment of the C16 amide, even though Pd/$ZrO_2$ removed 11 percentage points more nitrogen than the bare $ZrO_2$ in the hydrotreatment of the C16 amine. The activity and preference for HDO was reflected in the product distribution, which indicated that Pd/$ZrO_2$ preferentially converted the oxygen-containing intermediates. The findings emphasize the relative complexity of the C16 amide reaction network and the interference

of competitive HDO and HDN reactions in the hydrotreatment of molecules which contain both oxygen and nitrogen.

The tested catalysts exhibited activity for the formation of the C15 paraffin via the decarboxylation and decarbonylation routes in the C16 amide reaction network (Scheme 1, Figure 4). Even $Pt/ZrO_2$, which was the least selective catalyst for C–C bond cleavage, produced 10% of the C15 paraffin at full conversion (Figure 5a). In contrast, only $Ru/ZrO_2$ and $Rh/ZrO_2$ displayed a significant activity for the C–C bond cleavage of the C16 amine (Figure 6, Figure 7b), and the C15 paraffin yields were lower than in the C16 amide experiments. The C–C bond cleavage of the oxygen-containing compounds in the reaction network therefore appeared to be more favorable than the C–C bond cleavage of the C16 amine on the studied catalysts, which aligns with the findings by Di et al.[80]

## 4. Conclusions

In this work, $ZrO_2$-supported Pt, Pd, Rh, Ru and Ni catalysts were studied in the hydrotreatment of the C16 amide (*n*-hexadecanamide) and the C16 amine (1-hexadecylamine). $Ru/ZrO_2$ and $Pt/ZrO_2$ were the most active catalysts for the formation of *n*-paraffins from both model compounds, while $Pd/ZrO_2$ and $Ni/ZrO_2$ only displayed a modest activity at the studied reaction conditions.

The hydrotreatment of the C16 amide proceeded more efficiently than the hydrotreatment of the C16 amine on the studied catalysts, which was due to the activity of the Lewis acid sites of the $ZrO_2$ support for the conversion of the C16 amide. A high HDO activity was not always reflected in a high HDN activity. For example, $Rh/ZrO_2$ was highly active for oxygen removal via C–C bond cleavage routes in the C16 amide experiments, but only showed a low conversion and nitrogen removal in the HDN of the C16 amine.

The reaction network of the C16 amide was influenced both by the support and the activity and selectivity of the metals for the conversion of the oxygen-containing and nitrogen-containing intermediate products. The metal catalysts mainly differed in their tendency to catalyze condensation reactions and in their preference for C–C, C–O and C–N bond cleavage routes in the formation of the paraffins, which was reflected in the yields of the C32 condensation products, the C15 paraffin and the C16 paraffin. Characterization by CO and $H_2$ pulse chemisorption, XRD, XRF, $CO_2$-TPD, pyridine FTIR and $N_2$-physisorption could not explain the differences in the product distribution of the noble metal catalysts, which indicates that the metal identity and its influence on the adsorption strength, adsorption mode and transition states of the reactants and intermediate products accounted for the observed differences in the activity and selectivity. The low activity of the $Ni/ZrO_2$ catalyst may, however, have been due to the poor dispersion and/or incomplete reduction of Ni.

$Ru/ZrO_2$ and $Rh/ZrO_2$ were highly active for C–C bond cleavage routes and selectively formed the C15 paraffin in both the C16 amide and C16 amine hydrotreatment experiments. In case of the C16 amide, the C–C bond cleavage partly occurred from the oxygen-containing and nitrogen-containing intermediate products, but may also have occurred directly from the C16 amide. $Pt/ZrO_2$ was the only catalyst that was more selective for the formation of the C16 paraffin than the C15 paraffin from both model compounds, and the formation and decomposition of the C32 condensation products played an important role in reaction pathway towards the C16 paraffin. The C32 condensation products were likewise readily

produced by the low-activity $Pd/ZrO_2$ and $Ni/ZrO_2$ catalysts, whereas their formation was not preferred on $Ru/ZrO_2$ and $Rh/ZrO_2$, highlighting the mechanistic differences between the catalysts.

To our knowledge, the selective formation of $C_{n-1}$ normal paraffins via C–C bond cleavage routes has not been reported before in the hydrotreatment of fatty amides and amines. The finding aligns with recent HDO studies over supported noble metal catalysts and emphasizes the influence of the active metal on the activity and selectivity of different supported noble metal catalysts.

Supporting Information Available: Catalyst characterization data from $N_2$-physisorption, XRD, STEM and XPS measurements, additional activity test data

## Acknowledgement

Henni Kuokka is acknowledged for assistance with the batch reactor experiments. Dr. Hua Jiang and the facilities of the OtaNano Nanomicroscopy center are acknowledged for the STEM images. Dr. Yingnan Zhao and the Research Analytics department of Neste Corporation are acknowledged for the guidance and equipment support related to the pyridine FTIR measurements. This work used the Bioeconomy and Raw materials research infrastructures at Aalto University.

This work was funded by Neste Corporation as a part of the Neste-Aalto HDN catalyst development project.

## Notes

Non-disclosure agreement prevents researchers from disclosing conflict of interest.

# References

(1) Mortensen, P. M.; Grunwaldt, J.-D.; Jensen, P. A.; Knudsen, K. G.; Jensen, A. D. A Review of Catalytic Upgrading of Bio-Oil to Engine Fuels. *Appl. Catal., A* **2011**, *407*, 1–19. https://doi.org/10.1016/j.apcata.2011.08.046.

(2) De, S.; Saha, B.; Luque, R. Hydrodeoxygenation Processes: Advances on Catalytic Transformations of Biomass-Derived Platform Chemicals into Hydrocarbon Fuels. *Bioresour. Technol.* **2015**, *178*, 108–118. https://doi.org/10.1016/j.biortech.2014.09.065.

(3) Furimsky, E. Catalytic Hydrodeoxygenation. *Appl. Catal., A* **2000**, *199*, 147–190. https://doi.org/10.1016/S0926-860X(99)00555-4.
(4) Bu, Q.; Lei, H.; Zacher, A. H.; Wang, L.; Ren, S.; Liang, J.; Wei, Y.; Liu, Y.; Tang, J.; Zhang, Q.; Ruan, R. A Review of Catalytic Hydrodeoxygenation of Lignin-Derived Phenols from Biomass Pyrolysis. *Bioresour. Technol.* **2012**, *124*, 470–477. https://doi.org/10.1016/j.biortech.2012.08.089.
(5) Ding, S.; Parlett, C. M. A.; Fan, X. Recent Developments in Multifunctional Catalysts for Fatty Acid Hydrodeoxygenation as a Route towards Biofuels. *Mol. Catal.* **2021**, *523*, 111492. https://doi.org/10.1016/j.mcat.2021.111492.
(6) Rogers, K. A.; Zheng, Y. Selective Deoxygenation of Biomass-Derived Bio-Oils within Hydrogen-Modest Environments: A Review and New Insights. *ChemSusChem* **2016**, *9*, 1750–1772. https://doi.org/10.1002/cssc.201600144.
(7) Huber, G. W.; O'Connor, P.; Corma, A. Processing Biomass in Conventional Oil Refineries: Production of High Quality Diesel by Hydrotreating Vegetable Oils in Heavy Vacuum Oil Mixtures. *Appl. Catal., A* **2007**, *329*, 120–129. https://doi.org/10.1016/j.apcata.2007.07.002.
(8) Šimáček, P.; Kubička, D.; Šebor, G.; Pospíšil, M. Hydroprocessed Rapeseed Oil as a Source of Hydrocarbon-Based Biodiesel. *Fuel* **2009**, *88*, 456–460. https://doi.org/10.1016/j.fuel.2008.10.022.
(9) Madl, T.; Mittelbach, M. Quantification of Primary Fatty Acid Amides in Commercial Tallow and Tallow Fatty Acid Methyl Esters by HPLC-APCI-MS. *Analyst* **2005**, *130*, 565–570. https://doi.org/10.1039/b415779f.
(10) Palardy, O.; Behnke, C.; Laurens, L. M. L. Fatty Amide Determination in Neutral Molecular Fractions of Green Crude Hydrothermal Liquefaction Oils From Algal Biomass. *Energy Fuels* **2017**, *31*, 8275–8282. https://doi.org/10.1021/acs.energyfuels.7b01175.
(11) Chen, W.-T.; Tang, L.; Qian, W.; Scheppe, K.; Nair, K.; Wu, Z.; Gai, C.; Zhang, P.; Zhang, Y. Extract Nitrogen-Containing Compounds in Biocrude Oil Converted from Wet Biowaste via Hydrothermal Liquefaction. *ACS Sustainable Chem. Eng.* **2016**, *4*, 2182–2190. https://doi.org/10.1021/acssuschemeng.5b01645.
(12) Zimmermann, J.; Chiaberge, S.; Iversen, S. B.; Raffelt, K.; Dahmen, N. Sequential Extraction and Characterization of Nitrogen Compounds after Hydrothermal Liquefaction of Sewage Sludge. *Energy Fuels* **2022**, *36*, 14292–14303. https://doi.org/10.1021/acs.energyfuels.2c02622.
(13) Batalha, N.; Checa, R.; Lorentz, C.; Afanasiev, P.; Stańczyk, K.; Kapusta, K.; Laurenti, D.; Geantet, C. Lignite and Biomass Waste Hydrothermal Liquefaction Crude Upgrading by Hydrotreatment. *Energy Fuels* **2023**, *37*, 10506–10520. https://doi.org/10.1021/acs.energyfuels.3c01550.
(14) Heracleous, E.; Vassou, M.; Lappas, A. A.; Rodriguez, J. K.; Chiaberge, S.; Bianchi, D. Understanding the Upgrading of Sewage Sludge-Derived Hydrothermal Liquefaction Biocrude via Advanced Characterization. *Energy Fuels* **2022**, *36*, 12010–12020. https://doi.org/10.1021/acs.energyfuels.2c01746.
(15) Furimsky, E.; Massoth, F. E. Hydrodenitrogenation of Petroleum. *Catal. Rev.* **2005**, *47*, 297–489. https://doi.org/10.1081/CR-200057492.
(16) Castello, D.; Haider, M. S.; Rosendahl, L. A. Catalytic Upgrading of Hydrothermal Liquefaction Biocrudes: Different Challenges for Different Feedstocks. *Renew. Energy* **2019**, *141*, 420–430. https://doi.org/10.1016/j.renene.2019.04.003.
(17) Li, Z.; Savage, P. E. Feedstocks for Fuels and Chemicals from Algae: Treatment of Crude Bio-Oil over HZSM-5. *Algal Res.* **2013**, *2*, 154–163. https://doi.org/10.1016/j.algal.2013.01.003.
(18) López Barreiro, D.; Gómez, B. R.; Ronsse, F.; Hornung, U.; Kruse, A.; Prins, W. Heterogeneous Catalytic Upgrading of Biocrude Oil Produced by Hydrothermal Liquefaction of Microalgae: State of the Art and Own Experiments. *Fuel Process. Technol.* **2016**, *148*, 117–127. https://doi.org/10.1016/j.fuproc.2016.02.034.

(19) Biller, P.; Sharma, B. K.; Kunwar, B.; Ross, A. B. Hydroprocessing of Bio-Crude from Continuous Hydrothermal Liquefaction of Microalgae. *Fuel* **2015**, *159*, 197–205. https://doi.org/10.1016/j.fuel.2015.06.077.

(20) Zhu, C.; Gutiérrez, O. Y.; Santosa, D. M.; Flake, M.; Weindl, R.; Kutnyakov, I.; Shi, H.; Wang, H. Kinetics of Nitrogen-, Oxygen- and Sulfur-Containing Compounds Hydrotreating during Co-Processing of Bio-Crude with Petroleum Stream. *Appl. Catal., B* **2022**, *307*, 121197. https://doi.org/10.1016/j.apcatb.2022.121197.

(21) Liu, M.; Shi, Y.; Wu, K.; Liang, J.; Wu, Y.; Huang, S.; Yang, M. Upgrading of Palmitic Acid and Hexadecanamide over Co-Based Catalysts: Effect of Support ($SiO_2$, γ-$Al_2O_3$ and H-ZSM-22). *Catal. Commun.* **2019**, *129*, 105726. https://doi.org/10.1016/j.catcom.2019.105726.

(22) Snåre, M.; Kubičková, I.; Mäki-Arvela, P.; Eränen, K.; Murzin, D. Yu. Heterogeneous Catalytic Deoxygenation of Stearic Acid for Production of Biodiesel. *Ind. Eng. Chem. Res.* **2006**, *45*, 5708–5715. https://doi.org/10.1021/ie060334i.

(23) Malins, K. Synthesis of Renewable Hydrocarbons from Vegetable Oil Feedstock by Hydrotreatment over Selective Sulfur-Free $SiO_2$-$Al_2O_3$ Supported Monometallic Pd, Pt, Ru, Ni, Mo and Bimetallic NiMo Catalysts. *Fuel* **2021**, *285*, 119129. https://doi.org/10.1016/j.fuel.2020.119129.

(24) Furimsky, E. Hydroprocessing Challenges in Biofuels Production. *Catal. Today* **2013**, *217*, 13–56. https://doi.org/10.1016/j.cattod.2012.11.008.

(25) Meitzner, G. Metal-Catalyzed Reactions of Methylamine in the Presence of Hydrogen. *J. Catal.* **1986**, *98*, 513–521. https://doi.org/10.1016/0021-9517(86)90339-8.

(26) Marafi, M.; Furimsky, E. Hydroprocessing Catalysts Containing Noble Metals: Deactivation, Regeneration, Metals Reclamation, and Environment and Safety. *Energy Fuels* **2017**, *31*, 5711–5750. https://doi.org/10.1021/acs.energyfuels.7b00471.

(27) Verkama, E.; Albersberger, S.; Arandia, A.; Meinander, K.; Tiitta, M.; Karinen, R.; Puurunen, R. L. Hydrodeoxygenation and Hydrodenitrogenation of *n*-Hexadecanamide over Pt Catalysts: Effect of the Support. *Catal. Sci. Technol.* In press, **2024**. https://doi.org/10.1039/D3CY01480K

(28) Verkama, E.; Auvinen, P.; Albersberger, S.; Tiitta, M.; Karinen, R.; Puurunen, R. L. Competitive Hydrodeoxygenation and Hydrodenitrogenation Reactions in the Hydrotreatment of Fatty Acid and Amine Mixtures. *Top. Catal.* **2023**. *66*, 1353–1368. https://doi.org/10.1007/s11244-023-01784-w.

(29) Meitzner, G.; Mykytka, W. J.; Sinfelt, J. H. Kinetics of Hydrogenolysis of Methylamine on a Rhodium Catalyst. *Catal. Lett.* **1995**, *32*, 335–344. https://doi.org/10.1007/BF00813228.

(30) Migone, R. A.; Meitzner, G.; Mykytka, W. J.; Sinfelt, J. H. Kinetics of Methylamine Conversion on a Pd Catalyst in the Presence of $H_2$. *Catal. Lett.* **1995**, *31*, 27–35. https://doi.org/10.1007/BF00817030.

(31) Sinfelt, J. H. Catalytic Hydrogenolysis on Metals. *Catal. Lett.* **1991**, *9*, 159–171. https://doi.org/10.1007/BF00773174.

(32) Cattenot, M.; Peeters, E.; Geantet, C.; Devers, E.; Zotin, J. L. Mechanism of Carbon–Nitrogen Bond Scission in the Presence of $H_2S$ on Pt Supported Catalysts. *Catal. Lett.* **2005**, *99*, 171–176. https://doi.org/10.1007/s10562-005-2110-z.

(33) Almithn, A. S.; Hibbitts, D. D. Impact of Metal and Heteroatom Identities in the Hydrogenolysis of C–X Bonds (X = C, N, O, S, and Cl). *ACS Catal.* **2020**, *10*, 5086–5100. https://doi.org/10.1021/acscatal.0c00481.

(34) Li, M.-R.; Wang, G.-C. Differentiation of the C–O and C–C Bond Scission Mechanisms of 1-Hexadecanol on Pt(111) and Ru(0001): A First Principles Analysis. *Catal. Sci. Technol.* **2017**, *7*, 743–760. https://doi.org/10.1039/C6CY02529C.

(35) Kon, K.; Onodera, W.; Takakusagi, S.; Shimizu, K. Hydrodeoxygenation of Fatty Acids and Triglycerides by Pt-Loaded $Nb_2O_5$ Catalysts. *Catal. Sci. Technol.* **2014**, *4*, 3705–3712. https://doi.org/10.1039/C4CY00757C.

(36) Bie, Y.; Lehtonen, J.; Kanervo, J. Hydrodeoxygenation (HDO) of Methyl Palmitate over Bifunctional Rh/$ZrO_2$ Catalyst: Insights into Reaction Mechanism via Kinetic Modeling. *Appl. Catal., A* **2016**, *526*, 183–190. https://doi.org/10.1016/j.apcata.2016.08.030.

(37) Ni, J.; Leng, W.; Mao, J.; Wang, J.; Lin, J.; Jiang, D.; Li, X. Tuning Electron Density of Metal Nickel by Support Defects in Ni/$ZrO_2$ for Selective Hydrogenation of Fatty Acids to Alkanes and Alcohols. *Appl. Catal., B* **2019**, *253*, 170–178. https://doi.org/10.1016/j.apcatb.2019.04.043.

(38) Biller, P.; Ross, A. B. Potential Yields and Properties of Oil from the Hydrothermal Liquefaction of Microalgae with Different Biochemical Content. *Bioresour. Technol.* **2011**, *102*, 215–225. https://doi.org/10.1016/j.biortech.2010.06.028.

(39) Brunauer, S.; Emmett, P. H.; Teller, E. Adsorption of Gases in Multimolecular Layers. *J. Am. Chem. Soc.* **1938**, *60*, 309–319. https://doi.org/10.1021/ja01269a023.

(40) Barrett, E. P.; Joyner, L. G.; Halenda, P. P. The Determination of Pore Volume and Area Distributions in Porous Substances. I. Computations from Nitrogen Isotherms. *J. Am. Chem. Soc.* **1951**, *73*, 373–380. https://doi.org/10.1021/ja01145a126.

(41) Bergeret, G.; Gallezot, P. Particle Size and Dispersion Measurements. In *Handbook of Heterogeneous Catalysis*; John Wiley & Sons, Ltd, 2008; pp 738–765. https://doi.org/10.1002/9783527610044.hetcat0038.

(42) A. López-Benítez, G. Berhault, R. Silva-Rodrigo, J. A. Rodríguez-Ávila, M. Vrinat and A. Guevara-Lara, *Catal. Lett.* **2019**, *149*, 2656–2670. https://doi.org/10.1007/s10562-019-02831-6

(43) Powell, C. X-Ray Photoelectron Spectroscopy Database XPS, Version 4.1, NIST Standard Reference Database 20, 1989. https://doi.org/10.18434/T4T88K.

(44) Emeis, C. A. Determination of Integrated Molar Extinction Coefficients for Infrared Absorption Bands of Pyridine Adsorbed on Solid Acid Catalysts. *J. Catal.* **1993**, *141*, 347–354. https://doi.org/10.1006/jcat.1993.1145.

(45) de Saint Laumer, J.-Y.; Cicchetti, E.; Merle, P.; Egger, J.; Chaintreau, A. Quantification in Gas Chromatography: Prediction of Flame Ionization Detector Response Factors from Combustion Enthalpies and Molecular Structures. *Anal. Chem.* **2010**, *82*, 6457–6462. https://doi.org/10.1021/ac1006574.

(46) Thommes, M.; Kaneko, K.; Neimark, A. V.; Olivier, J. P.; Rodriguez-Reinoso, F.; Rouquerol, J.; Sing, K. S. W. Physisorption of Gases, with Special Reference to the Evaluation of Surface Area and Pore Size Distribution (IUPAC Technical Report). *Pure Appl. Chem.* **2015**, *87*, 1051–1069. https://doi.org/10.1515/pac-2014-1117.

(47) Behrens, M.; Schlögl, R. X-Ray Diffraction and Small Angle X-Ray Scattering. In *Characterization of Solid Materials and Heterogeneous Catalysts*; 2012; pp 609–653. https://doi.org/10.1002/9783527645329.ch15.

(48) Jia, X.; Zhang, X.; Rui, N.; Hu, X.; Liu, C. Structural Effect of Ni/$ZrO_2$ Catalyst on $CO_2$ Methanation with Enhanced Activity. *Appl. Catal., B* **2019**, *244*, 159–169. https://doi.org/10.1016/j.apcatb.2018.11.024.

(49) Tsiotsias, A. I.; Hafeez, S.; Charisiou, N. D.; Al-Salem, S. M.; Manos, G.; Constantinou, A.; AlKhoori, S.; Sebastian, V.; Hinder, S. J.; Baker, M. A.; Polychronopoulou, K.; Goula, M. A. Selective Catalytic Deoxygenation of Palm Oil to Produce Green Diesel over Ni Catalysts Supported on $ZrO_2$ and $CeO_2$–$ZrO_2$: Experimental and Process Simulation Modelling Studies. *Renew. Energy* **2023**, *206*, 582–596. https://doi.org/10.1016/j.renene.2023.02.038.

(50) Italiano, C.; Llorca, J.; Pino, L.; Ferraro, M.; Antonucci, V.; Vita, A. CO and $CO_2$ Methanation over Ni Catalysts Supported on $CeO_2$, $Al_2O_3$ and $Y_2O_3$ Oxides. *Appl. Catal., B* **2020**, *264*, 118494. https://doi.org/10.1016/j.apcatb.2019.118494.

(51) Omarov, Sh. O.; Sladkovskiy, D. A.; Martinson, K. D.; Peurla, M.; Aho, A.; Murzin, D. Yu.; Popkov, V. I. Influence of the Initial State of $ZrO_2$ on Genesis, Activity and Stability of Ni/$ZrO_2$ Catalysts for Steam Reforming of Glycerol. *Appl. Catal., A* **2021**, *616*, 118098. https://doi.org/10.1016/j.apcata.2021.118098.

(52) Batista, J.; Pintar, A.; Mandrino, D.; Jenko, M.; Martin, V. XPS and TPR Examinations of ɣ-Alumina-Supported Pd-Cu Catalysts. *Appl. Catal., A* **2001** *206*, 113–124. https://doi.org/10.1016/S0926-860X(00)00589-5

(53) Mäkelä, E.; Escobedo, J. L. G.; Neuvonen, J.; Lahtinen, J.; Lindblad, M.; Lassi, U.; Karinen, R.; Puurunen, R. L. Liquid-Phase Hydrodeoxygenation of 4-Propylphenol to Propylbenzene: Reducible Supports for Pt Catalysts. *ChemCatChem* **2020**, *12*, 4090–4104. https://doi.org/10.1002/cctc.202000429.

(54) Hoang, D. L.; Lieske, H. Effect of Hydrogen Treatments on $ZrO_2$ and Pt/$ZrO_2$ Catalysts. *Catal. Lett.* **1994**, *27*, 33–42. https://doi.org/10.1007/BF00806975.

(55) Wang, J. A.; López, T.; Bokhimi, X.; Novaro, O. Phase Composition, Reducibility and Catalytic Activity of Rh/Zirconia and Rh/Zirconia-Ceria Catalysts. *J. Mol. Catal. A: Chem.* **2005**, *239*, 249–256. https://doi.org/10.1016/j.molcata.2005.06.021.

(56) Fornasiero, P.; Dimonte, R.; Rao, G. R.; Kaspar, J.; Meriani, S.; Trovarelli, A.; Graziani, M. Rh-Loaded $CeO_2$-$ZrO_2$ Solid-Solutions as Highly Efficient Oxygen Exchangers: Dependence of the Reduction Behavior and the Oxygen Storage Capacity on the Structural-Properties. *J. Catal.* **1995**, *151*, 168–177. https://doi.org/10.1006/jcat.1995.1019.

(57) Eriksson, S.; Rojas, S.; Boutonnet, M.; Fierro, J. L. G. Effect of Ce-Doping on Rh/$ZrO_2$ Catalysts for Partial Oxidation of Methane. *Appl. Catal., A* **2007**, *326*, 8–16. https://doi.org/10.1016/j.apcata.2007.03.019.

(58) Coq, B.; Kumbhar, P. S.; Moreau, C.; Moreau, P.; Figueras, F. Zirconia-Supported Monometallic Ru and Bimetallic Ru-Sn, Ru-Fe Catalysts: Role of Metal Support Interaction in the Hydrogenation of Cinnamaldehyde. *J. Phys. Chem.* **1994**, *98*, 10180–10188. https://doi.org/10.1021/j100091a038.

(59) Jóźwiak, W. K. Influence of Reoxidation Temperature on TPR of Zirconia Supported Rhodium. *React Kinet Catal. Lett.* **1986**, *30*, 345–351. https://doi.org/10.1007/BF02064312.

(60) Mohamed, Z.; Dasireddy, V. D. B. C.; Singh, S.; Friedrich, H. B. $TiO_2$ and $ZrO_2$ Supported Ru Catalysts for CO Mitigation Following the Water-Gas Shift Reaction. *Int. J. Hydrogen Energy* **2018**, *43*, 22291–22302. https://doi.org/10.1016/j.ijhydene.2018.10.061.

(61) Wei, H.; Yan, X.; He, S.; Sun, C. Catalytic Wet Air Oxidation of Pentachlorophenol over Ru/$ZrO_2$ and Ru/$ZrSiO_2$ Catalysts. *Catal. Today* **2013**, *201*, 49–56. https://doi.org/10.1016/j.cattod.2012.07.004.

(62) Choque, V.; de la Piscina, P. R.; Molyneux, D.; Homs, N. Ruthenium Supported on New $TiO_2$–$ZrO_2$ Systems as Catalysts for the Partial Oxidation of Methane. *Catal. Today* **2010**, *149*, 248–253. https://doi.org/10.1016/j.cattod.2009.09.017.

(63) Valdés-Martínez, O. U.; Díaz de León, J. N.; Santolalla, C. E.; Talavera-López, A.; Avila-Paredes, H.; de los Reyes, J. A. Fundamental Study of Catalytic Functionalities Involved in Effective C–O Cleavage over Ru-Supported Catalysts. *Ind. Eng. Chem. Res.* **2021**, *60*, 18880–18890. https://doi.org/10.1021/acs.iecr.1c03058.

(64) Viinikainen, T.; Rönkkönen, H.; Bradshaw, H.; Stephenson, H.; Airaksinen, S.; Reinikainen, M.; Simell, P.; Krause, O. Acidic and Basic Surface Sites of Zirconia-Based Biomass Gasification Gas Clean-up Catalysts. *Appl. Catal., A* **2009**, *362*, 169–177. https://doi.org/10.1016/j.apcata.2009.04.037.

(65) Vo, D.-V. N.; Adesina, A. A. A Potassium-Promoted Mo Carbide Catalyst System for Hydrocarbon Synthesis. *Catal. Sci. Technol.* **2012**, *2*, 2066–2076. https://doi.org/10.1039/C2CY20385E.

(66) Busca, G. The Surface Acidity of Solid Oxides and Its Characterization by IR Spectroscopic Methods. An Attempt at Systematization. *Phys. Chem. Chem. Phys.* **1999**, *1*, 723–736. https://doi.org/10.1039/A808366E.

(67) Tamura, M.; Shimizu, K.; Satsuma, A. Comprehensive IR Study on Acid/Base Properties of Metal Oxides. *Appl. Catal., A* **2012**, *433–434*, 135–145. https://doi.org/10.1016/j.apcata.2012.05.008.
(68) Wu, P.; Tang, X.; He, Z.; Liu, Y.; Wang, Z. Alkali Metal Poisoning and Regeneration of Selective Catalytic Reduction Denitration Catalysts: Recent Advances and Future Perspectives. *Energy Fuels* **2022**, *36*, 5622–5646. https://doi.org/10.1021/acs.energyfuels.2c01036.
(69) Davidson, D.; Karten, M. The Pyrolysis of Amides. *J. Am. Chem. Soc.* **1956**, *78*, 1066–1068. https://doi.org/10.1021/ja01586a051.
(70) Cabrero-Antonino, J. R.; Adam, R.; Papa, V.; Beller, M. Homogeneous and Heterogeneous Catalytic Reduction of Amides and Related Compounds Using Molecular Hydrogen. *Nat. Commun.* **2020**, *11*, 3893. https://doi.org/10.1038/s41467-020-17588-5.
(71) Pestman, R.; van Duijne, A.; Pieterse, J. A. Z.; Ponec, V. The Formation of Ketones and Aldehydes from Carboxylic Acids, Structure-Activity Relationship for Two Competitive Reactions. *J. Mol. Catal. A: Chem.* **1995**, *103*, 175–180. https://doi.org/10.1016/1381-1169(95)00138-7.
(72) Pestman, R.; Koster, R. M.; Pieterse, J. A. Z.; Ponec, V. Reactions of Carboxylic Acids on Oxides: 1. Selective Hydrogenation of Acetic Acid to Acetaldehyde. *J. Catal.* **1997**, *168*, 255–264. https://doi.org/10.1006/jcat.1997.1623.
(73) Pestman, R.; Koster, R. M.; van Duijne, A.; Pieterse, J. A. Z.; Ponec, V. Reactions of Carboxylic Acids on Oxides: 2. Bimolecular Reaction of Aliphatic Acids to Ketones. *J. Catal.* **1997**, *168*, 265–272. https://doi.org/10.1006/jcat.1997.1624.
(74) Salvatore, R. N.; Yoon, C. H.; Jung, K. W. Synthesis of Secondary Amines. *Tetrahedron* **2001**, *57*, 7785–7811. https://doi.org/10.1016/S0040-4020(01)00722-0
(75) Greenfield, H. Catalytic Hydrogenation of Butyronitrile. *Ind. Eng. Chem. Prod. Res. Dev.* **1967**, *6*, 142–144. https://doi.org/10.1021/i360022a014.
(76) Adamczyk, A. J. First-Principles Analysis of Acetonitrile Reaction Pathways to Primary, Secondary, and Tertiary Amines on Pd(111). *Surf. Sci.* **2019**, *682*, 84–98. https://doi.org/10.1016/j.susc.2018.09.006.
(77) Sivasankar, N.; Prins, R. Reactions of Mixed Dialkyl- and Trialkylamines over Pd/γ-$Al_2O_3$. *J. Catal.* **2006**, *241*, 342–355. https://doi.org/10.1016/j.jcat.2006.04.032.
(78) Peng, B.; Zhao, C.; Kasakov, S.; Foraita, S.; Lercher, J. A. Manipulating Catalytic Pathways: Deoxygenation of Palmitic Acid on Multifunctional Catalysts. *Chem. Eur. J.* **2013**, *19*, 4732–4741. https://doi.org/10.1002/chem.201203110.
(79) Malins, K.; Malina, I. The Effects of Supported Pd, Pt, Re, Rh, Ru, Ir, Au, and Ni Catalysts on Renewable Hydrocarbon Production from Alternative Feedstock. *Biomass Bioenergy* **2023**, *171*, 106732. https://doi.org/10.1016/j.biombioe.2023.106732.
(80) Di, L.; Yao, S.; Li, M.; Wu, G.; Dai, W.; Wang, G.; Li, L.; Guan, N. Selective Catalytic Hydrogenolysis of Carbon–Carbon σ Bonds in Primary Aliphatic Alcohols over Supported Metals. *ACS Catal.* **2015**, *5*, 7199–7207. https://doi.org/10.1021/acscatal.5b02180.
(81) Sutton, J. E.; Vlachos, D. G. Ethanol Activation on Closed-Packed Surfaces. *Ind. Eng. Chem. Res.* **2015**, *54*, 4213–4225. https://doi.org/10.1021/ie5043374.
(82) Gürbüz, E. I.; Hibbitts, D. D.; Iglesia, E. Kinetic and Mechanistic Assessment of Alkanol/Alkanal Decarbonylation and Deoxygenation Pathways on Metal Catalysts. *J. Am. Chem. Soc.* **2015**, *137*, 11984–11995. https://doi.org/10.1021/jacs.5b05361.
(83) Bhogeswararao, S.; Srinivas, D. Catalytic Conversion of Furfural to Industrial Chemicals over Supported Pt and Pd Catalysts. *J. Catal.* **2015**, *327*, 65–77. https://doi.org/10.1016/j.jcat.2015.04.018.
(84) Boda, L.; Onyestyák, G.; Solt, H.; Lónyi, F.; Valyon, J.; Thernesz, A. Catalytic Hydroconversion of Tricaprylin and Caprylic Acid as Model Reaction for Biofuel Production from Triglycerides. *Appl. Catal., A* **2010**, *374*, 158–169. https://doi.org/10.1016/j.apcata.2009.12.005.

(85) Veriansyah, B.; Han, J. Y.; Kim, S. K.; Hong, S.-A.; Kim, Y. J.; Lim, J. S.; Shu, Y.-W.; Oh, S.-G.; Kim, J. Production of Renewable Diesel by Hydroprocessing of Soybean Oil: Effect of Catalysts. *Fuel* **2012**, *94*, 578–585. https://doi.org/10.1016/j.fuel.2011.10.057.

(86) Delbecq, F.; Sautet, P. Competitive C=C and C=O Adsorption of α-β-Unsaturated Aldehydes on Pt and Pd Surfaces in Relation with the Selectivity of Hydrogenation Reactions: A Theoretical Approach. *J. Catal.* **1995**, *152*, 217–236. https://doi.org/10.1006/jcat.1995.1077.

(87) Farneth, W. E.; Gorte, R. J. Methods for Characterizing Zeolite Acidity. *Chem. Rev.* **1995**, *95*, 615–635. https://doi.org/10.1021/cr00035a007.

(88) Li, J.; Zhang, J.; Wang, S.; Xu, G.; Wang, H.; Vlachos, D. G. Chemoselective Hydrodeoxygenation of Carboxylic Acids to Hydrocarbons over Nitrogen-Doped Carbon–Alumina Hybrid Supported Iron Catalysts. *ACS Catal.* **2019**, *9*, 1564–1577. https://doi.org/10.1021/acscatal.8b04967.

(89) Mills, G. A.; Steffgen, F. W. Catalytic Methanation. *Catal. Rev.* **1974**, *8*, 159–210. https://doi.org/10.1080/01614947408071860.

(90) Gao, J.; Liu, Q.; Gu, F.; Liu, B.; Zhong, Z.; Su, F. Recent Advances in Methanation Catalysts for the Production of Synthetic Natural Gas. *RSC Adv.* **2015**, *5*, 22759–22776. https://doi.org/10.1039/C4RA16114A.

(91) Berenblyum, A. S.; Danyushevsky, V. Ya.; Katsman, E. A.; Podoplelova, T. A.; Flid, V. R. Production of Engine Fuels from Inedible Vegetable Oils and Fats. *Pet. Chem.* **2010**, *50*, 305–311. https://doi.org/10.1134/S0965544110040080.

(92) Coeck, R.; Berden, S.; Vos, D. E. D. Sustainable Hydrogenation of Aliphatic Acyclic Primary Amides to Primary Amines with Recyclable Heterogeneous Ruthenium–Tungsten Catalysts. *Green Chem.* **2019**, *21*, 5326–5335. https://doi.org/10.1039/C9GC01310E.

(93) Johnson, D. F.; Wang, Y.; Parmeter, J. E.; Hills, M. M.; Weinberg, W. H. Chemisorption and Thermal Decomposition of Methylamine on the Ruthenium(001) Surface. *J. Am. Chem. Soc.* **1992**, *114*, 4279–4290. https://doi.org/10.1021/ja00037a036.

(94) Lv, C.-Q.; Li, J.; Ling, K.-C.; Shang, Z.-F.; Wang, G.-C. Methylamine Decomposition on Nickel Surfaces: A Density Functional Theory Study. *Surf. Sci.* **2010**, *604*, 779–787. https://doi.org/10.1016/j.susc.2010.01.027.

(95) Hwang, S. Y.; Kong, A. C. F.; Schmidt, L. D. Surface Chemistry of Carbon-Nitrogen Bonds on Rhodium(111). 1. Ethanedinitrile and Methylamine. *J. Phys. Chem.* **1989**, *93*, 8327–8333. https://doi.org/10.1021/j100363a011.

(96) Sinfelt, J. H. Specificity in Catalytic Hydrogenolysis by Metals. In *Advances in Catalysis*; Eley, D. D., Pines, H., Weisz, P. B., Eds.; Academic Press, 1973; Vol. 23, pp 91–119. https://doi.org/10.1016/S0360-0564(08)60299-0.

(97) Sinfelt, J. H.; Yates, D. J. C. Catalytic Hydrogenolysis of Ethane over the Noble Metals of Group VIII. *J. Catal.* **1967**, *8*, 82–90. https://doi.org/10.1016/0021-9517(67)90284-9.

# Supporting Information: Zirconia-supported Pt, Pd, Rh, Ru and Ni Catalysts in the Hydrotreatment of Fatty Amides and Amines

*Emma Verkama[1]*, Sylvia Albersberger[2], Kristoffer Meinander[3], Marja Tiitta[2†], Reetta Karinen[1], Riikka L. Puurunen[1]*

*[1]Department of Chemical and Metallurgical Engineering, School of Chemical Engineering, Aalto University, P.O. Box 16100, 00076 Aalto, Finland*
*[2]Neste Corporation, P.O. Box 310, 06101 Porvoo, Finland*
*[3]Department of Bioproducts and Biosystems, School of Chemical Engineering, Aalto University, P.O. Box 16300, 00076 Aalto, Finland*

*Present address:*
*†Hamari, Finland*

** Corresponding author:*
*Email: emma.verkama@aalto.fi*

## $N_2$-Physisorption Isotherms and Pore Size Distribution

Figure S1 displays the $N_2$-physisorption isotherms of the catalysts and the bare $ZrO_2$ support.

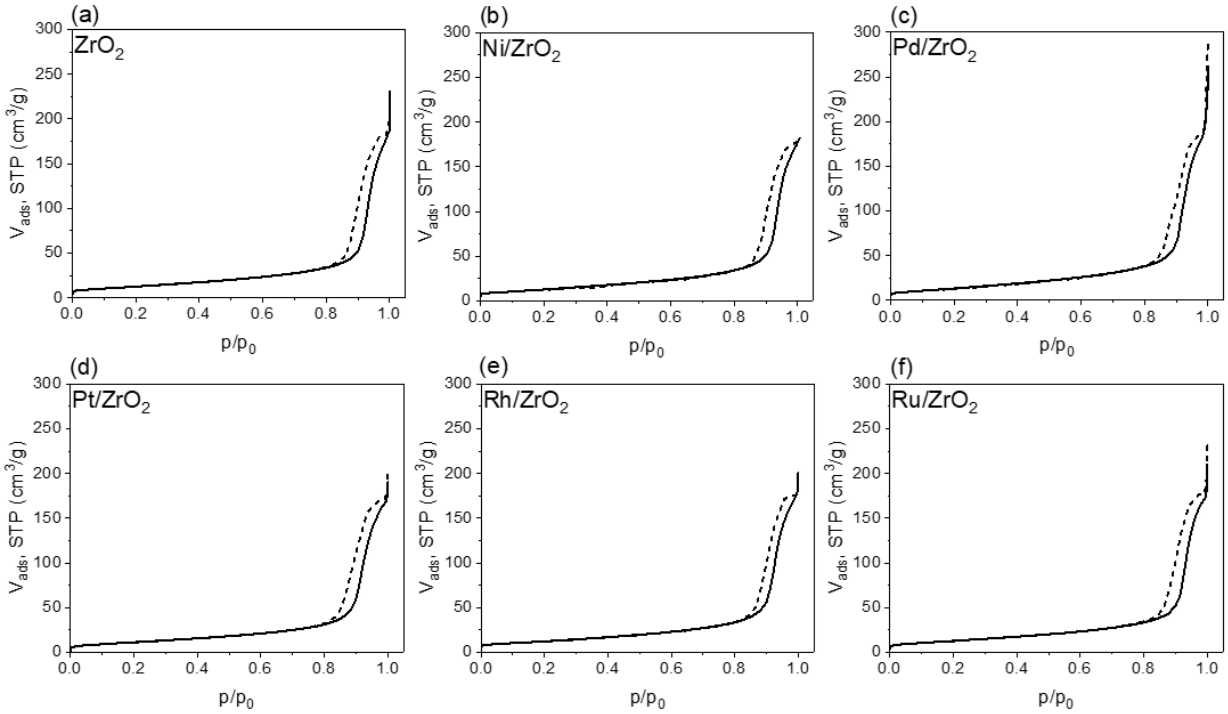


Figure S1. $N_2$-physisorpotion isotherms of (a) the bare $ZrO_2$ support and the calcined (b) $Ni/ZrO_2$, (c) $Pd/ZrO_2$, (d) $Pt/ZrO_2$, (e) $Rh/ZrO_2$ and (f) $Ru/ZrO_2$ catalysts.

Figure S2 displays the Barrett-Joyner-Halenda (BJH) pore size distribution of the catalysts and the bare $ZrO_2$ support.

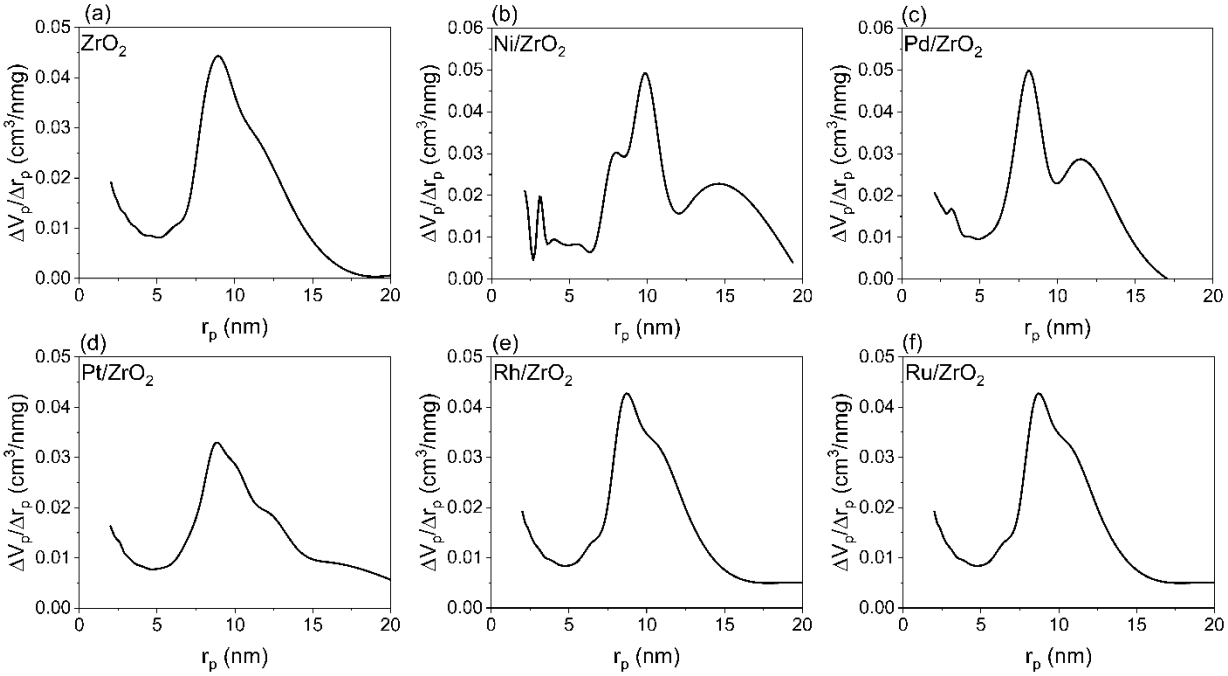


Figure S2. BJH pore size distribution of (a) the bare $ZrO_2$ support and the calcined (b) $Ni/ZrO_2$, (c) $Pd/ZrO_2$, (d) $Pt/ZrO_2$, (e) $Rh/ZrO_2$ and (f) $Ru/ZrO_2$ catalysts.

# X-ray Diffraction

The X-ray diffractograms of the calcined catalysts are presented in Figure S3.

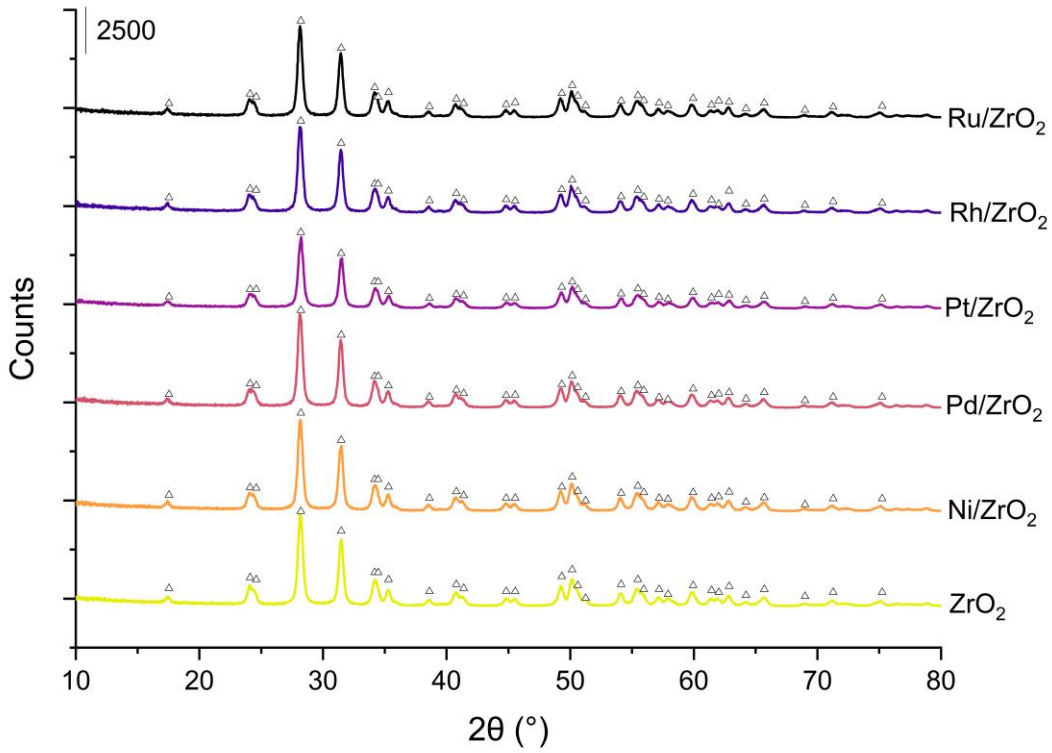


Figure S3. X-ray diffractograms of the calcined catalysts and the bare $ZrO_2$ support. The marked reflections (△) correspond to monoclinic $ZrO_2$ (ICDD 04-004-4339).

# Scanning Transmission Electron Microscopy

A selection of representative STEM images of the calcined catalysts, with corresponding elemental EDS mappings, is presented in Figure S4.

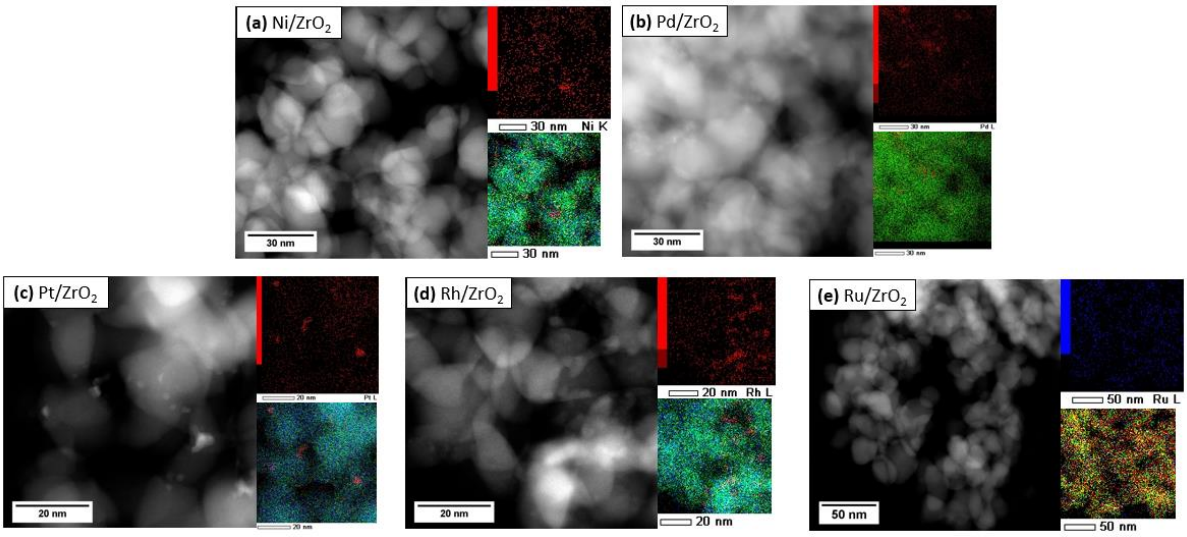


Figure S4. Representative STEM images and corresponding EDS mappings of the calcined (a) $Ni/ZrO_2$, (b) $Pd/ZrO_2$, (c) $Pt/ZrO_2$, (d) $Rh/ZrO_2$ and (e) $Ru/ZrO_2$ catalysts.

Table S1 presents the mean particle size and standard deviation of the mean particle size for the $Pt/ZrO_2$ and $Rh/ZrO_2$ catalysts, derived from STEM images. The particle size could not be reliably estimated from STEM images of the $Ru/ZrO_2$, $Pd/ZrO_2$ and $Ni/ZrO_2$ catalysts, due to an insufficient contrast between the active metal and the support.

Table S1. The mean metal particle size of the calcined Pt and Rh catalysts, derived from STEM images

| Catalyst | $d_{m,\,STEM}$ (nm) | Standard deviation, $d_{m,\,STEM}$ (nm) |
|---|---|---|
| $Pt/ZrO_2$ | 2.1 | 0.9 |
| $Rh/ZrO_2$ | 2.1 | 0.4 |

## X-ray Photoelectron Spectroscopy

The XPS survey spectra of the samples are presented in Figure S5. The samples were reduced ex situ at 350 °C in $H_2$ before the measurements and transferred to the equipment in atmosphere.

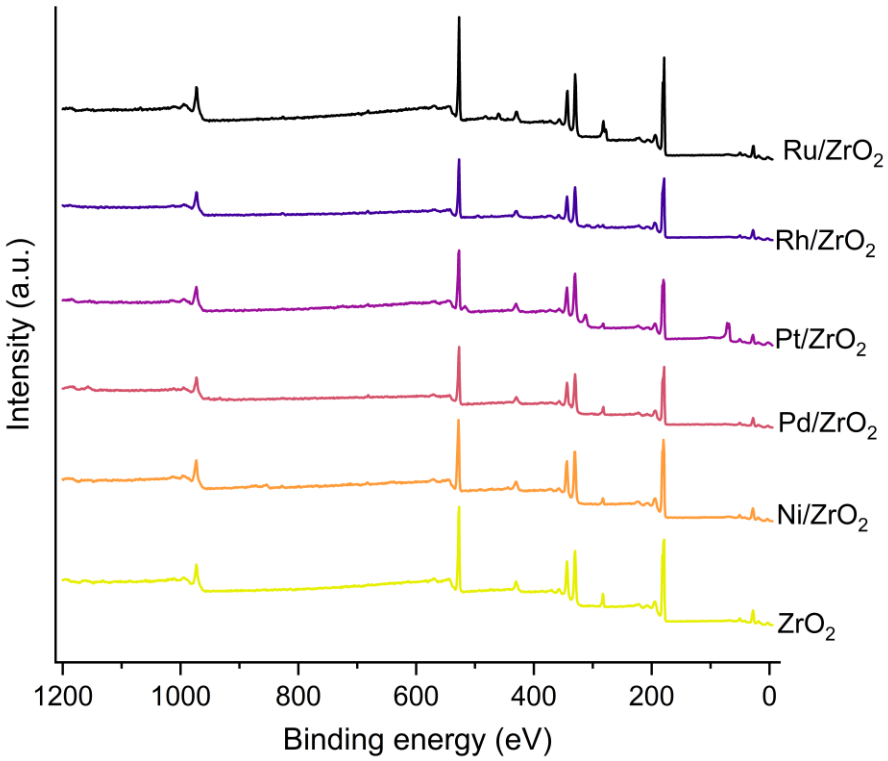


Figure S5. XPS survey spectra of the catalysts and the $ZrO_2$ support. The samples were reduced ex situ at 350 °C in $H_2$ before the measurements and transferred to the equipment in atmosphere.

The catalysts exhibited differences in the oxidation state of the $ZrO_2$ support and in the Zr 3d and O 1s binding energies, both relative to each other and to the bare $ZrO_2$. Table S2 presents the relative amounts of Zr in $ZrO_2$ and in a higher binding energy state. The higher binding energy component of Zr is herein referred to as the mixed state Zr oxide. Figure S6a displays the high resolution X-ray photoelectron spectra of the Zr 3d region for all catalysts and the $ZrO_2$ support, while the O 1s region is presented in Figure S6b.

Table S2. Relative amounts of Zr as $ZrO_2$ and in the mixed state Zr oxide, based on the XPS measurements

| Catalyst[a] | $ZrO_2$ (%) | Zr, mixed (%) |
|---|---|---|
| $ZrO_2$ | 96 | 6 |
| $Ni/ZrO_2$ | 78 | 22 |
| $Pd/ZrO_2$ | 87 | 13 |
| $Pt/ZrO_2$ | 84 | 16 |
| $Rh/ZrO_2$ | 85 | 15 |
| $Ru/ZrO_2$ | 88 | 12 |

[a]The samples were reduced ex situ in $H_2$ at 350 °C before the XPS measurements and transferred to the equipment in atmosphere.

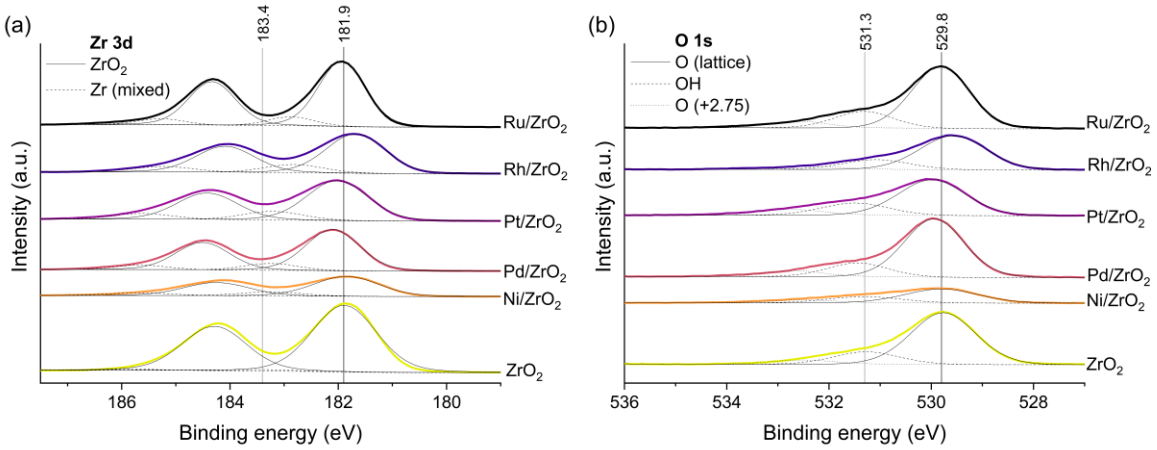


Figure S6. High resolution X-ray photoelectron spectra of the (a) Zr 3d and (b) O 1s regions. The binding energy of the main components of the bare $ZrO_2$ support have been indicated with vertical lines. The samples were reduced ex situ in $H_2$ at 350 °C before the XPS measurements and transferred to the equipment in atmosphere.

The Zr 3d and O 1s binding energies of the $ZrO_2$ support, $Ru/ZrO_2$ and $Ni/ZrO_2$ were similar (Figure S6). Meanwhile, the Zr 3d and O 1s binding energies of $Pt/ZrO_2$ and $Pd/ZrO_2$ were similar to each other and approximately 0.2 eV higher compared to the $ZrO_2$ support, suggesting that Pt and Pd may have withdrawn some electron density from the $ZrO_2$. $Rh/ZrO_2$ displayed approximately 0.3 eV lower Zr 3d and O 1s binding energies compared to the bare $ZrO_2$. Electron transfer from Rh to $ZrO_2$ may therefore have occurred, but it is also possible that the K present on the surface of $Rh/ZrO_2$ caused the shift. As seen from Table S2, the amount of the mixed state Zr oxide was considerably lower on the bare support (6.2%) compared to the catalysts (11.5-21.8%). The mixed state Zr oxide may be related to surface defects and to Zr bound to hydroxyl groups (Figure S6). Out of the catalysts, $Ni/ZrO_2$ had the highest relative amount of $ZrO_2$ in the mixed oxide state. The Zr 3d and O 1s binding energy shifts did not correlate with the relative amounts of Zr in the mixed oxide state in the samples.

## Catalytic Activity Tests

Figure S7 presents the product distribution of C16 amide experiments at similar conversion levels. The experiments were conducted at 300 °C and 80 bar $H_2$, using a reaction time of 30 min for $Pt/ZrO_2$ and 60 min for the other catalysts and the bare $ZrO_2$ support.

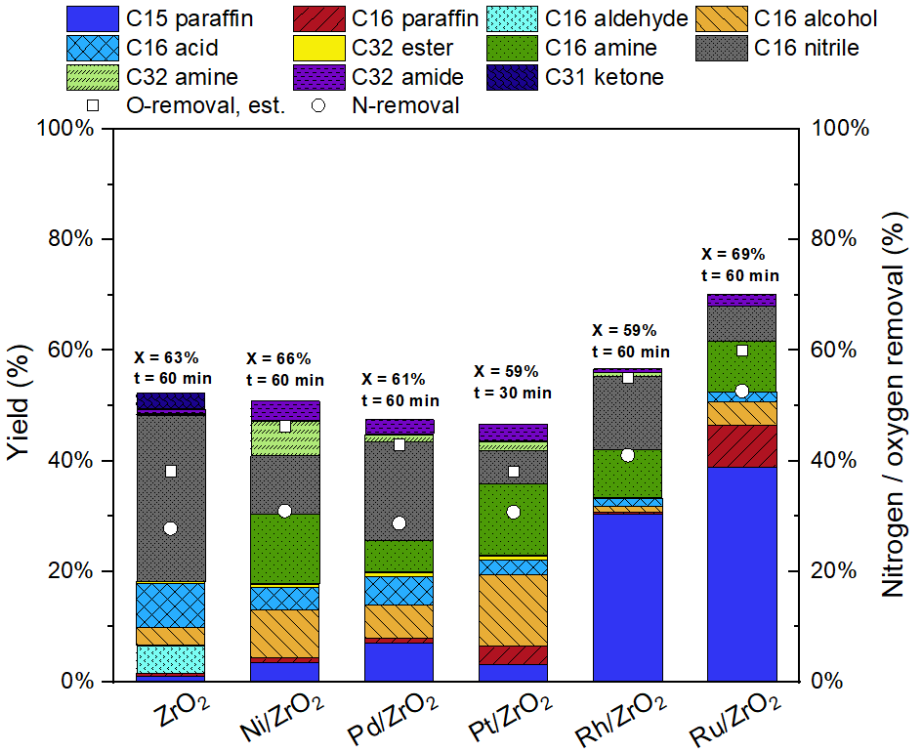


Figure S7. Product distribution, oxygen removal and nitrogen removal in the hydrotreatment of the C16 amide at 300 °C and 80 bar $H_2$, for the catalysts and the bare $ZrO_2$ support. The reaction time was 30 min for $Pt/ZrO_2$ and 60 min for the other materials.

Figure S8 presents the product distribution of $Pt/ZrO_2$ in the hydrotreatment of the C16 amide at low batch residence times (<0.5 $g_{cat}h/g_{amide}$).

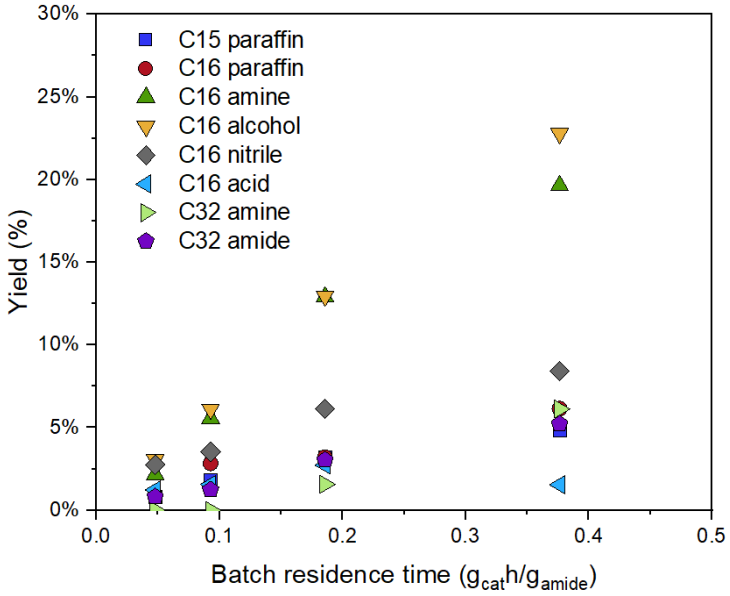


Figure S8. Product distribution of $Pt/ZrO_2$ in the hydrotreatment of the C16 amide as a function at batch residence time, for batch residence times below 0.5 $g_{cat}h/g_{amide}$. Reaction conditions: 300 °C, 80 bar $H_2$, 20 mg of catalyst, 100 ppm initial nitrogen content.